5. SITE 951[1]

Shipboard Scientific Party[2]

HOLE 951A

Date occupied: 11 August 1994

Date departed: 13 August 1994

Time on hole: 2 days, 2 hr, 49 min

Position: 32°1.896′N, 24°52.232′W

Bottom felt (drill-pipe measurement from rig floor, m): 5447.7

Distance between rig floor and sea level (m): 10.90

Water depth (drill-pipe measurement from sea level, m): 5436.8

Total depth (from rig floor, m): 5704.30

Penetration (m): 256.60

Number of cores (including cores having no recovery): 28

Total length of cored section (m): 256.60

Total core recovered (m): 251.5

Core recovery (%): 98

Oldest sediment cored:
Depth (mbsf): 256.60
Nature: clay with nannofossils
Earliest age: late Miocene

HOLE 951B

Date occupied: 13 August 1994

Date departed: 15 August 1994

Time on hole: 1 days, 14 hr, 19 min

Position: 32°1.895′N, 24°52.236′W

Bottom felt (drill-pipe measurement from rig floor, m): 5447.7

Distance between rig floor and sea level (m): 10.90

Water depth (drill-pipe measurement from sea level, m): 5436.8

Total depth (from rig floor, m): 5799.30

Penetration (m): 351.60

Number of cores (including cores having no recovery): 10

Total length of cored section (m): 96.60

Total core recovered (m): 84.6

Core recovery (%): 87.6

Oldest sediment cored:
Depth (mbsf): 351.60
Nature: clay
Earliest age: middle Miocene

Principal results: Site 951 is located in the northwestern Madeira Abyssal Plain at 32°1.90′N, 24°52.23′W, at a water depth of 5436.8 m in the Charis Fracture Zone Valley. Seismic profiles for the area show the same major units as at Site 950: an upper unit showing relatively high amplitude parallel reflectors that onlap onto basement highs, and a lower unit that drapes the basement highs. A third unit is present in the deepest part of the fracture zone and it shows reflectors with low coherency. The upper unit can be subdivided into three subunits by relatively strong reflectors at 180 ms and 235 ms. Reflectors within the lower two subunits are weaker than in the upper subunit. This seismic pattern, previously described by Searle (1987), is interpreted as pelagic drape over basement, with the deeper draped sequences being later infilled by rapidly accumulated turbidites.

In combination with the other two abyssal plain sites, the primary objective of this site was to determine the nature of the turbidite fill and to distinguish discrete sources for the various compositional groups of sediment flows. We aimed to correlate individual turbidite units between the three sites and tie them to the downhole log data and thereby to the extensive seismic profile network on the abyssal plain, which will enable mapping of individual flows or groups of flows, calculations of their volumes, and, in combination with the stratigraphic data, estimates of the amount of sediment contributed from each source since the inception of the plain. A secondary objective at all three sites involved determination of the long-term effects of sediment burial and diagenesis in a sequence of mixed volcanic, organic-rich, and organic-poor sediments.

Hole 951A was drilled to 255.6 mbsf and a total of 13 APC cores (0–118.8 mbsf) and 15 XCB cores (118.8–255.6 mbsf) were retrieved with average recovery rates of 98.6% and 97.5%, respectively. The hole was prematurely aborted when the XCB barrel became jammed inside the drill pipe. Hole 951B was washed down to 255 mbsf and drilling continued with the XCB barrel to 351.6 mbsf, recovering 10 cores with 87.6% average recovery rate.

The sedimentary sequence at Site 951 comprises only one lithologic unit that is comparable to Unit I at Site 950. This unit (0–351.6 mbsf) consists of Pleistocene to middle Miocene (0–13 Ma), thick clayey nannofossil mixed sediment, and nannofossil clay turbidites, interbedded with pelagic nannofossil oozes, mixed sediments, and clays. The unit has been subdivided into two subunits (Ia and Ib) based on the proportion of calcium carbonate in the pelagic interbeds. Below 123 mbsf (Unit Ib) the pelagic interbeds are all clays. The three primary types of turbidites seen at Site 950 are again present: volcaniclastic from the volcanic islands within the basin, organic-rich from the northwestern African margin, and calcareous from seamounts to the west of the plain. All three types are found throughout Unit I, but the occurrence of volcaniclastic turbidites is limited below 250 mbsf. Turbidites between 250–351.6 mbsf are dominated by the organic-rich type and show increasing amounts of siliceous microfossils downward. At Site 951 all three groups of turbidites are fine grained and only occasionally have silty bases, indicating the distal nature of each group. Again individual flows are separated by a few centimeters to decimeters of pelagic sediment indicating regular but infrequent deposition.

Preliminary AMS measurements have yielded a sedimentary bedding plane dominated fabric with sufficiently dissimilar maximum and intermediate susceptibility magnitudes that it should eventually be possible to establish flow directions within the various sedimentary units.

A magnetostratigraphy for the APC cores from this site yielded a sequence of reversal boundaries from C1n to C2An (Brunhes to the beginning of the Gauss), similar to those found at Site 950. Planktonic foraminifers provided useful biostratigraphic data from the pelagic inter-

[1] Schmincke, H.-U., Weaver, P.P.E., Firth, J.V., et al., 1995. *Proc. ODP, Init. Repts.*, 157: College Station, TX (Ocean Drilling Program).
[2] Shipboard Scientific Party is given in the list preceding the Table of Contents.

beds in the upper part of the hole (0–80 mbsf), below which they were only preserved in a few turbidite bases. Nannofossils, however, were found consistently in pelagic interbeds from 0–218 mbsf (0–6.5 Ma). Below this, turbidites were sampled to the base of each hole, but no FO were encountered. The deepest sediment examined at 351.13 mbsf contained *Reticulofenestra pseudoumbilicus* suggesting an age for the base of Hole 951B of less than 13.1 Ma.

Sediment accumulation rates for the pelagic interbeds average 4.4 m/m.y. from 0–2.6 Ma and 2.0 m/m.y. between 2.6–6.5 Ma. This change at 2.6 Ma is again caused by a deepening of the CCD at this time, allowing some calcium carbonate to be preserved through the late Pliocene and Pleistocene. The thickness of pelagic layers at Site 951 is 11.39 m compared to 14.6 m at Site 950. The reasons for this difference are not clear. The total sediment sequence has an accumulation rate of 33.8 m/m.y. from 0–6.5 Ma. Below this the absence of stratigraphic data precludes estimates of accumulation rates. Shore-based studies are expected to provide some data in this interval.

As at Site 950, carbonate, organic carbon, and sulfur data from both pelagic sediments and turbidites display major stratigraphic variation that facilitates the subdivision of the sequence. The data confirm that essentially synchronous regional changes in carbonate preservation occurred on the abyssal plain and in turbidite provenance areas during the late Miocene and the late Pliocene. The upper 250 m at Sites 950 and 951 may be correlated with a high degree of confidence. At both sites, organic-rich turbidites contain up to 2% C_{org} but they display less carbonate and higher sulfur below 220 mbsf. Carbon/nitrogen ratios again indicate that marine organic matter dominates in most beds.

A comprehensive suite of pore-water geochemical results were obtained from Site 951. Sulfate and ammonia data demonstrate that sulfate reduction is occurring principally in the deeper parts of the sequence below 150 mbsf. No evidence of significant methanogenesis is recorded in the sequence. Calcium and magnesium results suggest that precipitation of carbonate is occurring above and within the sulfate-reducing zone. Silica, potassium, and other pore-water data demonstrate that biogenic silica is being dissolved in the upper parts of the sequence, while diagenesis in the deeper section is related to clay mineral and zeolite formation. High pore-water silica and alkalinities below 250 mbsf coincide with an interval of organic-rich turbidites yielding diatoms and radiolarians that was not represented at Site 950. This emphasizes the role that lithology may play in controlling the distribution of pore-water species.

The physical properties from Site 951 show a close relationship to the lithologic units with high magnetic susceptibilities correlating with volcaniclastic turbidites. The downcore increase of GRAPE density, thermal conductivity, compressional-wave velocity, bulk density, and shear strength, as well as the downcore decrease of water content and porosity with depth, all suggest that the dominant process within the upper 200 mbsf is gravitational compaction. In contrast, grain density, a parameter normally with a small variation and no general depth trend, shows downcore variations that may result from changes in the chemical or mineralogical composition of the sediment.

Site 951 was not logged, but compared to the logging results at Site 950, the base of the upper seismic unit should have been at about 320 mbsf. This depth did not represent the base of the turbidite sequence, but a distinctive green to white turbidite with a coarse sandy base is present from 316.5 to 320.1 mbsf. The basal 2.4 m of this core (Core 157-951B-7X) was not recovered but could have consisted of similar sandy material. No other distinctive units were found above or below this turbidite.

The excellent core recovery at Site 951 will enable cross-correlation of individual turbidite units with the other two abyssal plain sites. Preliminary correlations can already be made between the thicker and more distinctive units, and the similar accumulation rates for Sites 950 and 951 indicate that there are few variations in thickness of individual beds between the two sites, even though they are over 59 nmi apart. This correlation will greatly aid mapping of individual units across the whole plain with the aid of seismic profiles. The sequence of organic-rich turbidites with high siliceous contents, encountered near the base of Site 951, however, may not correlate at all between the two sites. At present it is not certain whether these turbidites are equivalent in time to the lower organic-rich turbidites at Site 950 or whether they are older. Improved biostratigraphy should solve this problem.

BACKGROUND AND OBJECTIVES

Site 951 is the second of three sites on the Madeira Abyssal Plain aimed at determining the history of sediment mass wasting within the Canary Basin (see Fig. 1 of chapter "Site 950," this volume). It lies 59 nmi north of Site 950 in the Charis Fracture Zone Valley (Searle, 1987). This site should have remained open to the east through its history, and therefore it should have received all the major turbidity flows from the northwestern African margin and Canary Islands, in the same way as Site 950. The Charis Fracture Zone, however, leads westward toward the mid-Atlantic Ridge flank, and it does not open directly to the seamounts to the west. Thus the frequency of coarse calcareous turbidites derived from the seamounts is likely to be reduced, compared with the frequency at Site 950. All seismic reflectors are well developed at this site and the turbidite sequence has about the same thickness as at Site 950. Piston core data has shown that individual turbidites can be correlated across the plain (Weaver and Kuijpers, 1983) and it is expected that many flows found at Site 950 will also be recovered at Site 951. Variations in overall thickness of individual flows, together with coarseness of the basal layers will indicate the direction of entry onto the abyssal plain and thus a broad indication of the source area. In the calculation of volumes of individual flows it is important to distinguish basin-wide flows from smaller restricted flows. Because of its position near the northeastern entry point, a number of small flows are expected here that may not be present in the other sites. The data from this site will be integrated with data from the other two MAP sites to determine the volumes of individual turbidites and their emplacement ages.

Principal objectives include determination of the nature of the turbidite fill of the abyssal plain and identification of single turbidite units that can be correlated between the three abyssal plain sites. When tied to the downhole logging data from Sites 950 and 952 these units, or groups of units, will then be identifiable on the seismic profiles and correlated across the whole plain. This in turn will allow estimates of volumes of reworked sediment contributed to the abyssal plain through time. A secondary objective involves identifying the volcaniclastic turbidites and their frequencies to identify periods of instability on the Canary and Madeiran Islands.

UNDERWAY GEOPHYSICS

At the approach to Site 951 a 16-km-long single channel reflection seismic profile was obtained from 31°59′N, 24°57′W to 32°04′N, 24°49′W. The seismic source was an 80 $in.^3$ water gun. The signals were recorded on a single channel streamer and recorded digitally on 8 mm tape with a sample distance of 1 ms. The profile was plotted on line in two different scales on line-scan printers. The data was processed with shipboard SIOSEIS software. The processing sequence was as follows: bandpass filter (60–120 Hz), automatic gain control (500 ms window), finite difference migration, bandpass filter (60–120 Hz), tracemix (weights 1 2 1), and display on Versatec plotter (Fig. 1).

The sediments were penetrated to an ill-defined acoustic basement that is thought to represent the surface of the oceanic crust. The basement forms a deep depression located in the Charis Fracture Zone (Searle, 1987). The southern flank of the depression can be followed from the deepest part at a depth of about 1.2 s up to the seafloor and a further 300 ms above the seafloor.

The sedimentary fill in the depression is divided into major Units A, B, and C, as shown in Figure 1. The upper unit (A) stands out because of its regular reflector pattern. Numerous highly continuous re-

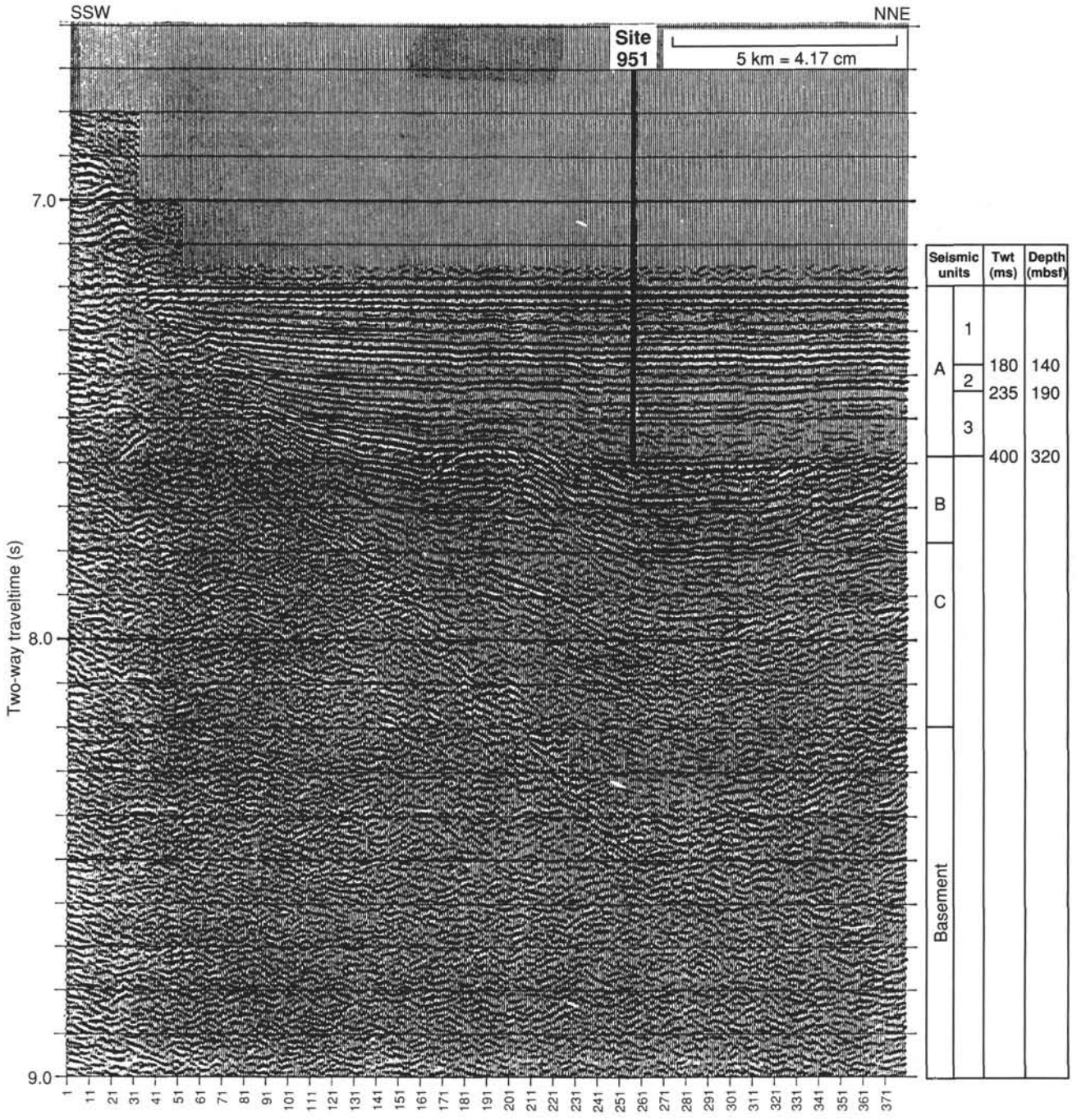

Figure 1. Processed seismic profile acquired during approach to Site 951. The two-way traveltimes and depths (in ms and mbsf) refer to Site 951.

flectors dominate the unit. The reflectors are parallel in the basin and converge as they onlap the basement. Unit B is characterized by a few high-amplitude reflectors (at some places interrupted), which separate intervals with chaotic patterns. In the lowermost unit (C) reflectors are few and with low coherency. Reflectors toplap the base of Unit B. A vague internal basin-and-fill structure is seen in the central part of the unit.

At Site 951 Unit A is divided into Subunits A1, A2, and A3. Subunit A1 is characterized by many high-amplitude reflectors and a central interval with relative low amplitudes and chaotic patterns. Subunit A2 is mainly transparent with a strong pair of reflectors near the base. The major part of Subunit A3 is almost transparent in the deeper part of the basin, but reflectors appear toward the side of the basin.

At Site 951 no logs were run. The depths given in Figure 1 are estimated from the depth vs. two-way traveltime relation obtained at Site 950.

OPERATIONS

Site 950 to Site 951 Transit

As soon as the main propulsion was commanded ahead, the drive coupling between propulsion motors P13A and P15A disintegrated,

scattering metal fragments that damaged motor P13A. The vessel was cautiously underway with only two of the six propulsion motors on the starboard shaft by 0040, local time, 11 August.

The 59 nmi transit to the MAP-4 area was made at an average speed of only 9 kt because of the reduced shaft horsepower. At 0615, 11 August, the seismic gear was deployed and a short survey was conducted over the site. The gear was retrieved and the hydrophones and thrusters were lowered as the vessel was moved on location according to GPS coordinates. The beacon was deployed after reaching the desired position.

Hole 951A (MAP-4)

The standard short-collar APC/XCB BHA used on the previous site was made up without the lockable float valve (LFV) and run to 5443 mbrf. Based upon a PDR depth of 5449.4 m, the first piston core was shot at 5447 mbrf and recovered 4.9 m of nannofossil ooze, establishing the mud line depth for this hole at 5436.8 mbsl.

APC coring advanced to 118.8 mbsf (Table 1) and recovered 117.2 m (98.6% recovery). The last two piston core liners (Cores 12H and 13H) were twisted and crushed, indicating that the liners were exposed to extreme suction while being extracted from the sticky clay of the formation. We decided to continue coring with the XCB assembly. Cores 3H to 13H were oriented.

Coring continued with the XCB assembly with excellent results. The hole was prematurely aborted when the XCB core barrel became jammed inside the drill pipe 366 m below the rig floor. The barrel was being retrieved after successfully cutting Core 157-951A-28X and was nearly home when the assistant driller noticed that the wire had "cross-wrapped" on the drum. The reaction was to immediately stop and reverse the direction of the winch, which was sudden enough to cause the core barrel inertia to carry the barrel into the sinker bars. The net effect parted the shear pin and at the same time jammed the barrel in the pipe approximately 366 mbrf.

After 1.5 hr of vain attempts to free the barrel, the top drive was set back and the pipe was pulled up enough so that the joint with the core barrel could be laid down. Because the length of the pull-out exceeded the depth of Hole 951A, the hole was terminated when the bit cleared the mud line at 1140UTC, 13 August. Coring with the XCB penetrated 137.8 m with 134.3 m recovered (97.5%). The total recovery on the hole was 251.5 m or 98.0% of the cored interval.

To prevent recurrence of this incident, a policy was introduced requiring the core-winch operator to bring the core winch to a complete stop before reversing the direction whenever a cross-wrap is observed. This procedure should prevent the core barrel from impacting the sinker bars.

Hole 951B

After the bit cleared the mud line at 1140, 1.5 hr were spent with the routine task of cutting and slipping 115 ft of drilling line. While this operation was underway, the vessel was offset 10 m south of Hole 951A. At 1450, 13 August, Hole 951B was spudded and drilled to 255 mbsf. After drilling at an average ROP of 85.0 m/hr, the wash barrel was retrieved and a core barrel was dropped at 2215, 13 August. XCB coring resumed on Site 951 and continued to 351.6 mbsf. A total of 10 cores were obtained with 87.6% recovery after penetrating 96.6 m.

LITHOSTRATIGRAPHY

The sedimentary sequence recovered at Site 951 comprises 351.6 m of alternating clayey nannofossil mixed sediment, nannofossil clay, clay with nannofossils, and clay with siliceous microfossils (interpreted as turbidites) with nannofossil oozes, mixed sediment, and clays (interpreted as pelagic sediments). The sequence ranges in age from Pleistocene to mid–late Miocene. Following a division comparable to that used for Site 950, only one unit (Unit I) is defined at Site 951, and it is subdivided into two subunits (Ia and Ib). These subunits are distinguished based on the clay content of the pelagic interbeds and the boundary between Subunits Ia and Ib is placed at 123 mbsf, below which pelagic interbeds are exclusively clays, and above which they are clays, clayey nannofossil mixed sediment, and nannofossil oozes (Fig. 2).

Subunit Ia

Interval: Sections 157-951A-1H-1 to 157-951A-14X-3
Depth: 0–123 mbsf

Subunit Ia contains a sequence of medium to very thick beds of green, gray, and grayish-green clayey nannofossil mixed sediment, and white clayey nannofossil ooze, commonly interbedded with thin to medium thick beds of nannofossil ooze and nannofossil clay mixed sediment. As described for Site 950, the medium to thick bedded units represent deposition from large-scale turbidity currents.

Pelagic Beds

The lower boundary of Subunit Ia is marked by a sharp change in the lithology of the pelagic intervals, from a mixture of clays, nannofossil oozes, and mixed sediment, to dominantly clays or clays with nannofossils. This change, at approximately at 120 mbsf, coincides with a significant decrease in the $CaCO_3$ of the pelagic intervals (Fig. 3). In general, the pelagic sediments are characterized by variable bioturbation ranging from minor to intense. Purple mottling is common. The lower contact is usually gradational toward the underlying turbidite. Smear slides indicate that the major calcareous components are nannofossils, foraminifers (whole and fragments), and carbonate particles, giving carbonate percentages up to 92%.

Turbidite Beds

Organic-rich and volcanic turbidites (for description see chapter "Site 950," "Lithostratigraphy" section, this volume) dominate in thickness and frequency over the calcareous and intermediate turbidites within Subunit Ia (Fig. 4). In general, the turbidites are characterized by thick intervals of homogeneous mud but may have parallel laminated (Fig. 5) or massive silty bases that are centimeters to decimeters in thickness. Commonly the upper contacts are slightly to heavily bioturbated, but lower contacts are sharp (Fig. 6). The vertical extent of bioturbation is variable, but in the organic-rich and volcanic turbidites it is usually no deeper than the position of an oxidation front, as defined by a sharp change in color. Both organic and volcanic turbidites commonly have two-tone coloration caused by oxidation of the upper part, which results in a lighter color in the uppermost part of individual turbidites. Downward remobilization of metals that concentrate at specific levels (Wilson et al., 1986; Thomson et al., 1987) can result in colorful laminae from yellow and orange to purple. Diffuse or well-defined purple laminae of probable chemical origin are common through the whole sedimentary column. The typical sediment color in the organic turbidites is light green in the upper part, and olive green or dark olive green below the oxidation front. In the volcanic turbidites, the contrast is not so well marked, but many have a distinctly lighter upper part that is interpreted to be the result of oxidation.

Petrographically, the turbidite muds (clayey nannofossil mixed sediment) are composed of clay minerals, coccolith plates, and minor silt-sized particles (mainly quartz, feldspar, mica, pyroxene, amphibole, glauconite, dolomite, opaque minerals, volcanic glass, zeolite, and siliceous microfossils). Additionally, silty and sandy bases of turbidites contain complete and fragmented planktonic and, more rarely,

Table 1. Coring summary, Holes 951A and 951B.

Core	Date (August 1994)	Time (UTC)	Sub-bottom (m) Top	Sub-bottom (m) Bottom	Cored (m)	Recovered (m)	Recovery (%)	Section	Length (m)	Depth (mbsf) Top	Depth (mbsf) Bottom	Samples
157-951A-												
1H	12	2105	0.0	4.8	4.8	4.88	101.0					
								1	1.50	0.00	1.50	
								2	1.50	1.50	3.00	IW 145–150
								3	1.50	3.00	4.50	HS 0–5
								CC	0.38	4.50	4.88	
2H	12	2230	4.8	14.3	9.5	9.79	103.0					
								1	1.50	4.80	6.30	
								2	1.50	6.30	7.80	
								3	1.50	7.80	9.30	
								4	1.50	9.30	10.80	IW 145–150
								5	1.50	10.80	12.30	HS 0–5
								6	1.50	12.30	13.80	
								7	0.61	13.80	14.41	
								CC	0.18	14.41	14.59	
3H	12	2345	14.3	23.8	9.5	9.71	102.0					
								1	1.50	14.30	15.80	Split liner
								2	1.50	15.80	17.30	
								3	1.50	17.30	18.80	
								4	1.50	18.80	20.30	IW 145–150
								5	1.50	20.30	21.80	HS 0–5
								6	0.50	21.80	22.30	
								7	0.64	22.30	22.94	
								8	0.86	22.94	23.80	
								CC	0.21	23.80	24.01	
4H	12	0120	23.8	33.3	9.5	9.34	98.3					
								1	1.50	23.80	25.30	
								2	1.50	25.30	26.80	
								3	1.50	26.80	28.30	
								4	1.50	28.30	29.80	IW 145–150
								5	1.50	29.80	31.30	HS 0–5
								6	1.50	31.30	32.80	
								7	0.25	32.80	33.05	
								CC	0.09	33.05	33.14	
5H	12	0250	33.3	42.8	9.5	9.81	103.0					
								1	1.50	33.30	34.80	
								2	1.50	34.80	36.30	
								3	1.50	36.30	37.80	
								4	1.50	37.80	39.30	IW 145–150
								5	1.50	39.30	40.80	HS 0–5
								6	1.50	40.80	42.30	
								7	0.61	42.30	42.91	
								CC	0.20	42.91	43.11	
6H	12	0405	42.8	52.3	9.5	9.24	97.2					
								1	1.50	42.80	44.30	
								2	1.50	44.30	45.80	
								3	1.50	45.80	47.30	
								4	1.50	47.30	48.80	IW 145–150
								5	1.50	48.80	50.30	HS 0–5
								6	1.50	50.30	51.80	
								CC	0.24	51.80	52.04	
7H	12	0530	52.3	61.8	9.5	8.87	93.3					
								1	1.50	52.30	53.80	
								2	1.50	53.80	55.30	
								3	1.50	55.30	56.80	
								4	1.50	56.80	58.30	IW 145–150
								5	1.50	58.30	59.80	HS 0–5
								6	1.18	59.80	60.98	
								CC	0.19	60.98	61.17	
8H	12	0650	61.8	71.3	9.5	8.90	93.7					
								1	1.50	61.80	63.30	
								2	1.50	63.30	64.80	
								3	1.00	64.80	65.80	Split liner
								4	1.50	65.80	67.30	
								5	1.50	67.30	68.80	IW 145–150
								6	1.50	68.80	70.30	HS 0–5
								7	0.22	70.30	70.52	
								CC	0.18	70.52	70.70	
9H	12	0815	71.3	80.8	9.5	9.62	101.0					
								1	1.50	71.30	72.80	
								2	1.50	72.80	74.30	
								3	1.50	74.30	75.80	
								4	1.50	75.80	77.30	IW 145–150
								5	1.50	77.30	78.80	HS 0–5
								6	1.50	78.80	80.30	
								7	0.51	80.30	80.81	
								CC	0.11	80.81	80.92	
10H	12	0935	80.8	90.3	9.5	9.60	101.0					
								1	1.50	80.80	82.30	
								2	1.50	82.30	83.80	
								3	1.50	83.80	85.30	
								4	1.50	85.30	86.80	
								5	1.50	86.80	88.30	IW 145–150
								6	1.50	88.30	89.80	HS 0–5
								7	0.60	89.80	90.40	
								CC	0.00	90.40	90.40	

Table 1 (continued).

Core	Date (August 1994)	Time (UTC)	Sub-bottom (m) Top	Sub-bottom (m) Bottom	Cored (m)	Recovered (m)	Recovery (%)	Section	Length (m)	Depth (mbsf) Top	Depth (mbsf) Bottom	Samples
11H	12	1045	90.3	99.8	9.5	9.57	101.0					
								1	1.50	90.30	91.80	
								2	1.50	91.80	93.30	
								3	1.50	93.30	94.80	
								4	1.50	94.80	96.30	
								5	1.50	96.30	97.80	
								6	1.50	97.80	99.30	HS 0–5
								CC	0.57	99.30	99.87	
12H	12	1205	99.8	109.3	9.5	9.07	95.5					
								1	1.50	99.80	101.30	Disturbed
								2	1.50	101.30	102.80	
								3	0.99	102.80	103.79	
								4	1.50	103.79	105.29	
								5	1.50	105.29	106.79	
								6	0.22	106.79	107.01	
								7	1.20	107.01	108.21	Disturbed
								CC	0.66	108.21	108.87	
13H	12	1320	109.3	118.8	9.5	8.78	92.4					
								1	1.50	109.30	110.80	
								2	1.50	110.80	112.30	
								3	1.50	112.30	113.80	
								4	0.93	113.80	114.73	35 cm lost in liner
								5	1.50	114.73	116.23	
								6	1.50	116.23	117.73	
								CC	0.00	117.73	117.73	
14X	12	1520	118.8	125.0	6.2	7.16	115.0					
								1	1.50	118.80	120.30	
								2	1.50	120.30	121.80	
								3	1.50	121.80	123.30	IW 145–150
								4	1.50	123.30	124.80	HS 0–5
								5	0.80	124.80	125.60	
								CC	0.36	125.60	125.96	
15X	12	1635	125.0	131.2	6.2	7.42	119.0					
								1	1.50	125.00	126.50	
								2	1.50	126.50	128.00	
								3	1.50	128.00	129.50	
								4	1.50	129.50	131.00	HS 0–5
								5	1.16	131.00	132.16	
								CC	0.26	132.16	132.42	
16X	12	1800	131.2	140.8	8.6	9.73	113.0					
								1	1.50	131.20	132.70	
								2	1.50	132.70	134.20	
								3	1.50	134.20	135.70	
								4	1.50	135.70	137.20	IW 145–150
								5	1.50	137.20	138.70	HS 0–5
								6	1.50	138.70	140.20	
								7	0.44	140.20	140.64	
								CC	0.29	140.64	140.93	
17X	12	1915	140.8	150.5	9.7	9.76	100.0					
								1	1.50	140.80	142.30	
								2	1.50	142.30	143.80	
								3	1.50	143.80	145.30	
								4	1.50	145.30	146.80	
								5	1.50	146.80	148.30	
								6	1.50	148.30	149.80	HS 0–5
								7	0.49	149.80	150.29	
								CC	0.27	150.29	150.56	
18X	12	2035	150.5	160.1	9.6	9.90	103.0					
								1	1.50	150.50	152.00	
								2	1.50	152.00	153.50	
								3	1.50	153.50	155.00	
								4	1.50	155.00	156.50	IW 140–150
								5	1.50	156.50	158.00	HS 0–5
								6	1.50	158.00	159.50	
								7	0.51	159.50	160.01	
								CC	0.39	160.01	160.40	
19X	12	2200	160.1	169.8	9.7	9.94	102.0					
								1	1.50	160.10	161.60	
								2	1.50	161.60	163.10	
								3	1.50	163.10	164.60	
								4	1.50	164.60	166.10	
								5	1.50	166.10	167.60	HS 0–5
								6	1.50	167.60	169.10	
								7	0.53	169.10	169.63	
								CC	0.41	169.63	170.04	
20X	12	2320	169.8	179.4	9.6	9.92	103.0					
								1	1.50	169.80	171.30	
								2	1.50	171.30	172.80	
								3	1.50	172.80	174.30	
								4	1.50	174.30	175.80	IW 140–150
								5	1.50	175.80	177.30	HS 0–5
								6	1.50	177.30	178.80	
								7	0.56	178.80	179.36	
								CC	0.36	179.36	179.72	
21X	13	0040	179.4	189.1	9.7	8.95	92.2					
								1	1.50	179.40	180.90	

Table 1 (continued).

Core	Date (August 1994)	Time (UTC)	Sub-bottom (m) Top	Sub-bottom (m) Bottom	Cored (m)	Recovered (m)	Recovery (%)	Section	Length (m)	Depth (mbsf) Top	Depth (mbsf) Bottom	Samples
								2	1.50	180.90	182.40	
								3	1.50	182.40	183.90	
								4	1.50	183.90	185.40	
								5	1.50	185.40	186.90	HS 0–5
								6	0.93	186.90	187.83	
								CC	0.52	187.83	188.35	
22X	13	0155	189.1	198.7	9.6	9.92	103.0					
								1	1.50	189.10	190.60	
								2	1.50	190.60	192.10	
								3	1.50	192.10	193.60	
								4	1.50	193.60	195.10	IW 140–150
								5	1.50	195.10	196.60	HS 0–5
								6	1.50	196.60	198.10	
								7	0.51	198.10	198.61	
								CC	0.41	198.61	199.02	
23X	13	0320	198.7	208.4	9.7	7.61	78.4					
								1	1.50	198.70	200.20	
								2	1.50	200.20	201.70	
								3	1.50	201.70	203.20	
								4	1.50	203.20	204.70	
								5	1.18	204.70	205.88	Shattered liner
								CC	0.43	205.88	206.31	
24X	13	0450	208.4	218.0	9.6	9.53	99.3					
								1	1.50	208.40	209.90	
								2	1.50	209.90	211.40	
								3	1.50	211.40	212.90	
								4	1.50	212.90	214.40	
								5	1.50	214.40	215.90	HS 0–5
								6	1.50	215.90	217.40	
								CC	0.53	217.40	217.93	
25X	13	0620	218.0	227.7	9.7	9.95	102.0					
								1	1.50	218.00	219.50	
								2	1.50	219.50	221.00	
								3	1.50	221.00	222.50	
								4	1.50	222.50	224.00	IW 140–150
								5	1.50	224.00	225.50	HS 0–5
								6	1.50	225.50	227.00	
								7	0.48	227.00	227.48	
								CC	0.47	227.48	227.95	
26X	13	0800	227.7	237.3	9.6	8.85	92.2					
								1	1.50	227.70	229.20	
								2	1.50	229.20	230.70	
								3	1.50	230.70	232.20	
								4	1.50	232.20	233.70	
								5	1.50	233.70	235.20	HS 0–5
								6	1.04	235.20	236.24	
								CC	0.31	236.24	236.55	
27X	13	0935	237.3	247.0	9.7	5.78	59.6					
								1	1.50	237.30	238.80	
								2	1.50	238.80	240.30	
								3	1.50	240.30	241.80	HS 0–5
								4	0.44	241.80	242.24	
								CC	0.84	242.24	243.08	
28X	13	1400	247.0	256.6	9.6	9.92	103.0					
								1	1.50	247.00	248.50	
								2	1.50	248.50	250.00	
								3	1.50	250.00	251.50	
								4	1.50	251.50	253.00	IW 140–150
								5	1.50	253.00	254.50	HS 0–5
								6	1.50	254.50	256.00	
								7	0.54	256.00	256.54	
								CC	0.38	256.54	256.92	
Coring totals					256.6	251.5	98.0					
157-851B-												
1X	13	0150	255.0	264.6	9.6	9.87	103.0					
								1	1.50	255.00	256.50	
								2	1.50	256.50	258.00	
								3	1.50	2568.00	259.50	
								4	1.50	259.50	261.00	
								5	1.50	261.00	262.50	HS 0–5
								6	1.50	262.50	264.00	
								7	0.48	264.00	264.40	
								CC	0.39	264.48	264.87	
2X	13	0345	264.6	274.3	9.7	3.36	34.6					
								1	0.98	264.60	265.58	5.2 m water-filled void between Sections 1 and 2
								2	1.50	265.58	267.08	
								3	0.56	267.08	267.64	
								CC	0.32	267.64	267.96	
3X	13	0510	274.3	283.9	9.6	6.67	69.5					
								1	1.50	274.30	275.80	
								2	1.50	275.80	277.30	
								3	1.50	277.30	278.80	IW 140–150
								4	1.50	278.80	280.30	HS 0–5
								5	0.35	280.30	280.65	
								CC	0.32	280.65	280.97	

Table 1 (continued).

Core	Date (August 1994)	Time (UTC)	Sub-bottom (m) Top	Sub-bottom (m) Bottom	Cored (m)	Recovered (m)	Recovery (%)	Section	Length (m)	Depth (mbsf) Top	Depth (mbsf) Bottom	Samples
4X	13	0640	283.9	293.6	9.7	8.41	86.7					
								1	1.50	283.90	285.40	
								2	1.50	285.40	286.90	
								3	1.50	286.90	288.40	
								4	1.50	288.40	289.90	
								5	1.50	289.90	291.40	HS 0–5
								6	0.56	291.40	291.96	
								CC	0.35	291.96	292.31	
5X	13	0815	293.6	303.2	9.6	9.92	103.0					
								1	1.50	293.60	295.10	
								2	1.50	295.10	296.60	
								3	1.50	296.60	298.10	
								4	1.51	298.10	299.61	
								5	1.50	299.61	301.11	HS 0–5
								6	1.50	301.11	302.61	
								7	0.50	302.61	303.11	
								CC	0.42	303.11	303.53	
6X	13	0945	303.2	312.9	9.7	9.89	102.0					
								1	1.50	303.20	304.70	
								2	1.50	304.70	306.20	
								3	1.50	306.20	307.70	
								4	1.50	307.70	309.20	IW 140–150
								5	1.50	309.20	310.70	HS 0–5
								6	1.50	310.70	312.20	
								7	0.49	312.20	312.69	
								CC	0.40	312.69	313.09	
7X	13	1100	312.9	322.5	9.6	7.17	74.7					
								1	1.50	312.90	314.40	
								2	1.50	314.40	315.90	
								3	1.50	315.90	317.40	
								4	1.50	317.40	318.90	HS 0–5
								5	1.00	318.90	319.90	
								CC	0.17	319.90	320.07	
8X	13	1225	322.5	332.1	9.6	9.86	103.0					
								1	1.50	322.50	324.00	
								2	1.50	324.00	325.50	
								3	1.50	325.50	327.00	
								4	1.50	327.00	328.50	
								5	1.50	328.50	330.00	
								6	1.50	330.00	331.50	HS 0–5
								7	0.48	331.50	331.98	
								CC	0.38	331.98	332.36	
9X	13	1405	332.1	341.9	9.8	9.77	99.7					
								1	1.50	332.10	333.60	
								2	1.50	333.60	335.10	
								3	1.50	335.10	336.60	IW 140–150
								4	1.50	336.60	338.10	HS 0–5
								5	1.50	338.10	339.60	
								6	1.50	339.60	341.10	
								7	0.50	341.10	341.60	
								CC	0.27	341.60	341.87	
10X	13	1545	341.9	351.6	9.7	9.61	99.1					
								1	1.50	341.90	343.40	
								2	1.50	343.40	344.90	
								3	1.50	344.90	346.40	
								4	1.50	346.40	347.90	HS 0–5
								5	1.50	347.90	349.40	
								6	1.50	349.40	350.90	
								CC	0.61	350.90	351.51	
Coring totals					96.6	84.6	87.6					

Notes: Hole 951A located at 32°1.896′N, 24°52.232′W. Water depth from sea surface = 5436.8 m. Hole 951B located at 32°1.895′N, 24°52.236′W. Water depth from sea surface = 5436.8 m.

benthic foraminifers and calcareous debris. The $CaCO_3$ content is relatively constant for the four types of turbidites within Subunit Ia: 40%–60% for the organic-rich, 50%–80% for the volcanic, greater than 70% for the calcareous, and close to 50% for the intermediate (Fig. 3). Variation in $CaCO_3$ content of the organic-rich (green) turbidites is reflected in their color, with lighter shades of green corresponding to greater $CaCO_3$.

Tephra Layer

A ~1-cm-thick bioturbated tephra fall layer in Section 157-951A-6H-2, at 71 cm, consists of greater than 95% clear glass shards dominantly with bubble wall morphologies. Most glass shards are ~100 µm in diameter, but some elongated pipe vesicle shards range up to 400 µm in length. A few thicker shards are pale brown. Trace amounts of feldspar and biotite occur as subhedral crystals up to 200 µm long. In addition, there are minor amounts of nannofossils (<5%) that were probably introduced through bioturbation.

Subunit Ib

Interval: Sections 157-951A-14X-4 to 157-951B-10X-CC
Depth: 123–353.2 mbsf

Thick and medium bedded turbidite units in Subunit Ib are separated by thin bedded clays or clay with nannofossils, which are interpreted as pelagic intervals.

Pelagic Beds

As discussed above, the distinction between Subunits Ia and Ib is based on the $CaCO_3$ content of the pelagic beds, which in Subunit Ib

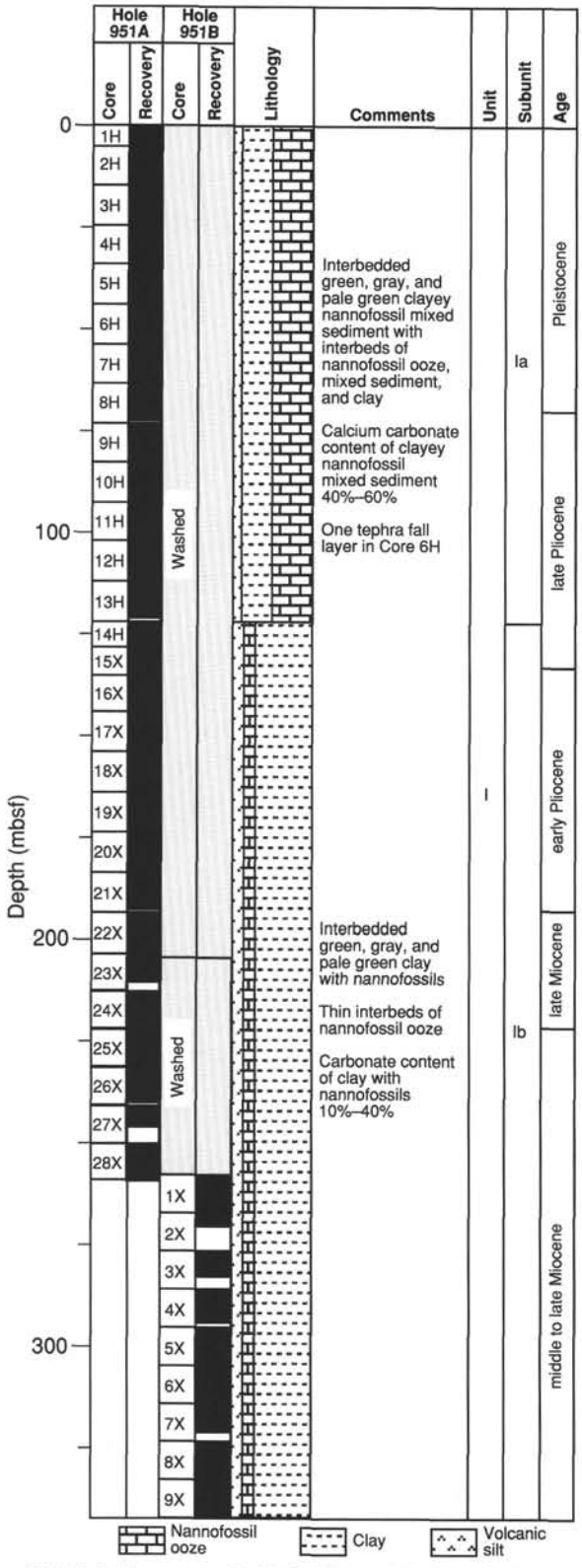

Figure 2. Lithologic summary for Holes 951A and 951B, showing the main lithologic units identified with age and a generalized graphic lithology.

are identified as predominantly nannofossil clay or clay with nannofossils ($CaCO_3 < 40\%$). As a consequence of their reduced carbonate content, the thickness of pelagic intervals decreases relative to Subunit Ia and their color becomes darker. Also, they more often show purplish mottling.

Turbidite Beds

Some important differences in the character of the turbidite beds and their composition relative to Subunit Ia include the following: the thickness and number of the intermediate and volcanic turbidites approximate those of the green turbidites for the interval 157-951A-14X-4 to 157-951A-28X-2. From 157-951A-28X-3 through to the base of Hole 951B, the sediments consist almost entirely of green units accompanied by an increase in siliceous microfossils (Figs. 4 and 7). The green turbidites are characterized by a contrasting and sharp change of color from bluish-green in the upper, oxic part to dark green in the lower, reduced part. One of the green turbidites (Sections 157-951B-8X-6, 7, and CC, and 157-951B-9X-1, 2, and 3) contains a 6.1-m-thick sandy base composed of quartz, feldspar, mica, rutile, foraminifers, calcareous fragments, and glass shards (Fig. 8).

Within Subunit Ib the percentage of $CaCO_3$ decreases markedly below 220 mbsf in both the organic and volcanic turbidites (Fig. 3). The organic-rich turbidites decrease from an average of 40%–60% (i.e., nannofossil clay mixed sediment) to less than 40% $CaCO_3$ (nannofossil clay or clay with nannofossils). The volcanic turbidites decrease from 50%–70% to less than 30%, although fewer samples were analyzed.

In Sections 157-951B-7X-4 and 157-951B-7X-5, a distinctive turbidite grades in color from pale white at the base to greenish gray at the top; it is 250 cm thick and has a finely laminated silty base. This is the only unit at Site 951 that exhibits a completely gradational change in color over its whole length and it can be correlated to a unit with similar characteristics at Site 950 (Core 157-950A-34X).

Depositional History

The depositional history of Site 951 is similar to that of Site 950 but with some important differences. From the late Miocene to the present, sedimentation at this site was dominated by the influx of large turbidity currents that intermittently laid down thick units (up to several meters) of very fine-grained sediments. These turbidity currents were derived from the northwestern African margin (green turbidites), the volcanic islands of Madeira and the Canaries (gray turbidites), and seamounts west of the Madeira Abyssal Plain (white, carbonate turbidites). These influxes of enormous volumes of sediment interrupted the background pelagic sedimentation.

Calcium carbonate determinations of pelagic interbeds indicate that there was a progressive deepening of the CCD in the late Pliocene with deposition of predominantly carbonate-poor pelagic sediment through the mid–late Miocene and early part of the Pliocene (transition of Subunit Ia to Subunit Ib). The organic-rich turbidites below 255 mbsf in Hole 951B contain siliceous microfossils, notably diatoms. Similar turbidites were not encountered in the lower part of Site 950. The lowermost section of Site 951 was dominated by organic-rich turbidites and the transition to red clays, as observed at Site 950, was not intersected. In addition, the distinctive calcarenite deposited at Site 950 (Unit II) was not found at Site 951 suggesting that this site was far enough away from the western seamount source to be isolated from coarse, proximal carbonate turbidites carrying shallow-water material.

During the latest Pliocene and Pleistocene, glacial-interglacial variations resulted in changes in the corrosiveness of bottom waters in the Madeira Abyssal Plain. Glacial periods were characterized by corrosive bottom waters, resulting in the deposition of relatively car-

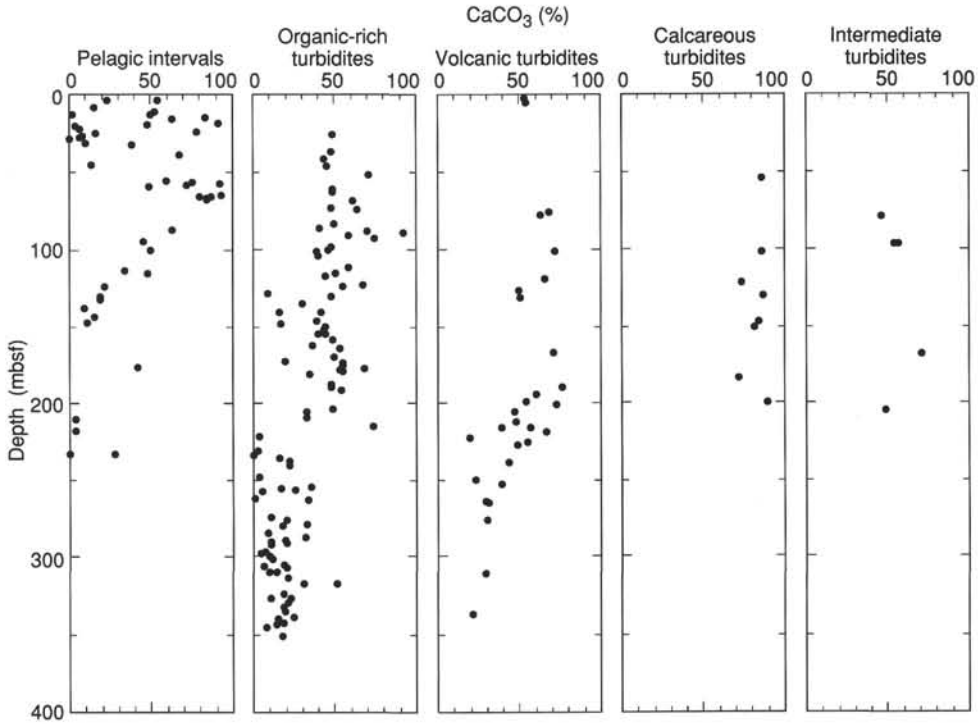

Figure 3. Downcore plot of calcium carbonate content through Unit I at Site 951 (Hole 951A = 0–256 mbsf, Hole 951B = 256–351 mbsf). Pelagic intervals include clays, mixed sediments, and oozes. The four types of turbidites (organic-rich, volcanic, calcareous, and intermediate) and the pelagic intervals are plotted separately to show their specific variations.

bonate poor sediment between major turbidite units, whereas interglacial periods favored the deposition of more carbonate-rich sediments.

BIOSTRATIGRAPHY

Introduction

Sediments ranging from Pleistocene to no older than middle Miocene were penetrated at Site 951 (Fig. 9). Holes 951A and 951B encountered predominantly turbidites with thin interbedded hemipelagic units. Because of this sediments were sampled from split core.

In hemipelagic sediments, planktonic foraminifers were present down to 79.43 mbsf (Sample 157-951A-9H-6, 62–64 cm), while autochthonous calcareous nannofossils were recovered down to 217.58 mbsf (Sample 157-951A-25X-5, 44.5 cm). Below 217.58 mbsf hemipelagic sediments were barren of nannofossils, so turbidites were sampled below this depth, which reduces the biostratigraphic resolution but provides maximum ages.

There is good agreement between nannofossil and foraminifer age and zonal assignments within the resolution of the shipboard sampling (Fig. 9). The placement of the Pleistocene/Pliocene boundary in Hole 951A is based on the evaluation of several factors. The work of Weaver and Clement (1986) in the cool subtropical region of the central North Atlantic Ocean and Weaver and Raymo (1989) in the eastern equatorial Atlantic Ocean indicates that the first occurrence of *Globorotalia truncatulinoides* can be used in this area to approximate the Pliocene/Pleistocene boundary (see Table 3 of the "Explanatory Notes" chapter, this volume). The cool subtropical waters at Site 951 apparently exclude taxa useful in warmer regions, specifically, *Globigerinoides fistulosus* and *Globorotalia tumida.* Sample 157-951A-8H-6, 75–77 cm, at 67.82 mbsf contains *G. truncatulinoides,* while Sample 157-951A-8H-6, 75–77 cm, at 69.55 mbsf does not. Therefore, the boundary is placed between 67.82 and 69.55 mbsf. This is in relatively good agreement with the nannofossil data, which have the consistent and common Pliocene marker *Discoaster brouweri* in Sample 157-951A-8H-5, 45.5 cm, at 67.76 mbsf, slightly above the first occurrence of *G. truncatulinoides.* Rather than use the highest occurrence of *D. brouweri,* which could be reworked, the lowest occurrence of *G. truncatulinoides* was used to approximate the boundary.

The Pliocene/Miocene boundary is placed between 187.20 and 188.83 mbsf (Sample 157-951A-21X-6, 29.5 cm, and Sample 157-951A-21X-CC, 1 cm) based on the highest occurrence of *Discoaster quinqueramus.*

Calcareous Nannofossils

Pleistocene

Well-preserved and abundant Pleistocene nannofossils were recovered from Samples 157-951A-1H-3, 119.5 cm (4.2 mbsf), to 157-951A-7H-5, 63 cm (58.93 mbsf) (Table 2). *Emiliania huxleyi* was present in Sample 157-951A-1H-3, 119.5 cm (4.2 mbsf); however *Gephyrocapsa* spp. were more dominant than *E. huxleyi,* indicating the sample is below the acme of *E. huxleyi* and is therefore older than 82,000 yr (Thierstein et al., 1977). The presence of *E. huxleyi* was difficult to determine in Sample 157-951A-2H-6, 83 cm, so it was given a broad assignment of Zones CN15 to CN14b. Shore-based electron microscope study will improve this assignment. Sample 157-951A-3H-7, 8 cm (22.38 mbsf), contains abundant *Pseudoemiliania lacunosa,* and it is only tentatively placed in Zone CN14a because the sediment was a turbidite and *P. lacunosa* could be reworked. Sample 157-951A-4H-4, 18 cm (28.48 mbsf), is confidently placed in Zone CN14a, as the sample is a hemipelagic ooze containing *P. lacunosa.* Sample 157-951A-4H-6, 18 cm (31.48

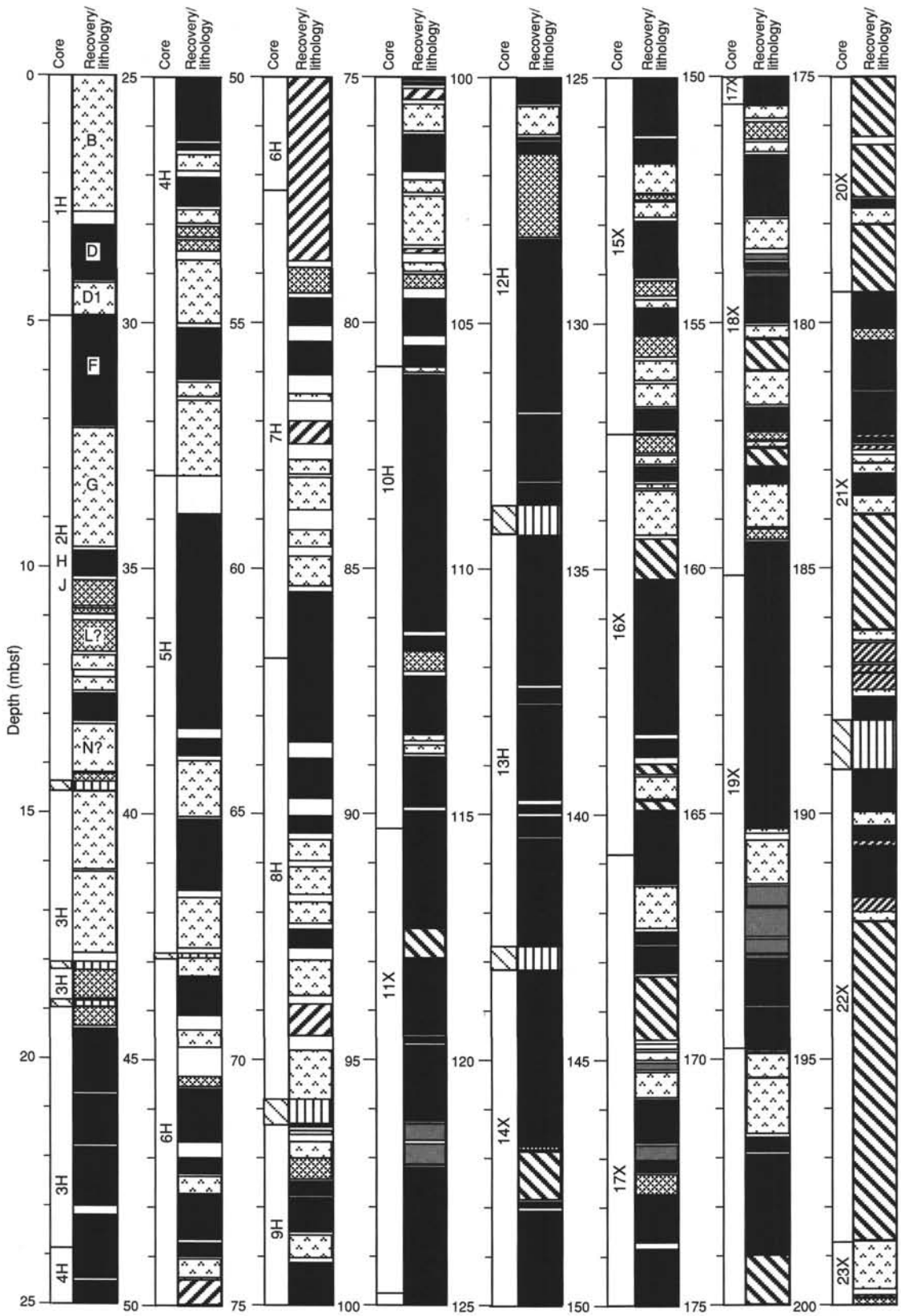

Figure 4. Genetic log of the sedimentary succession cored at Site 951 showing the occurrence of individual turbidites, their compositional type, and the position of pelagic interbeds within the sequence.

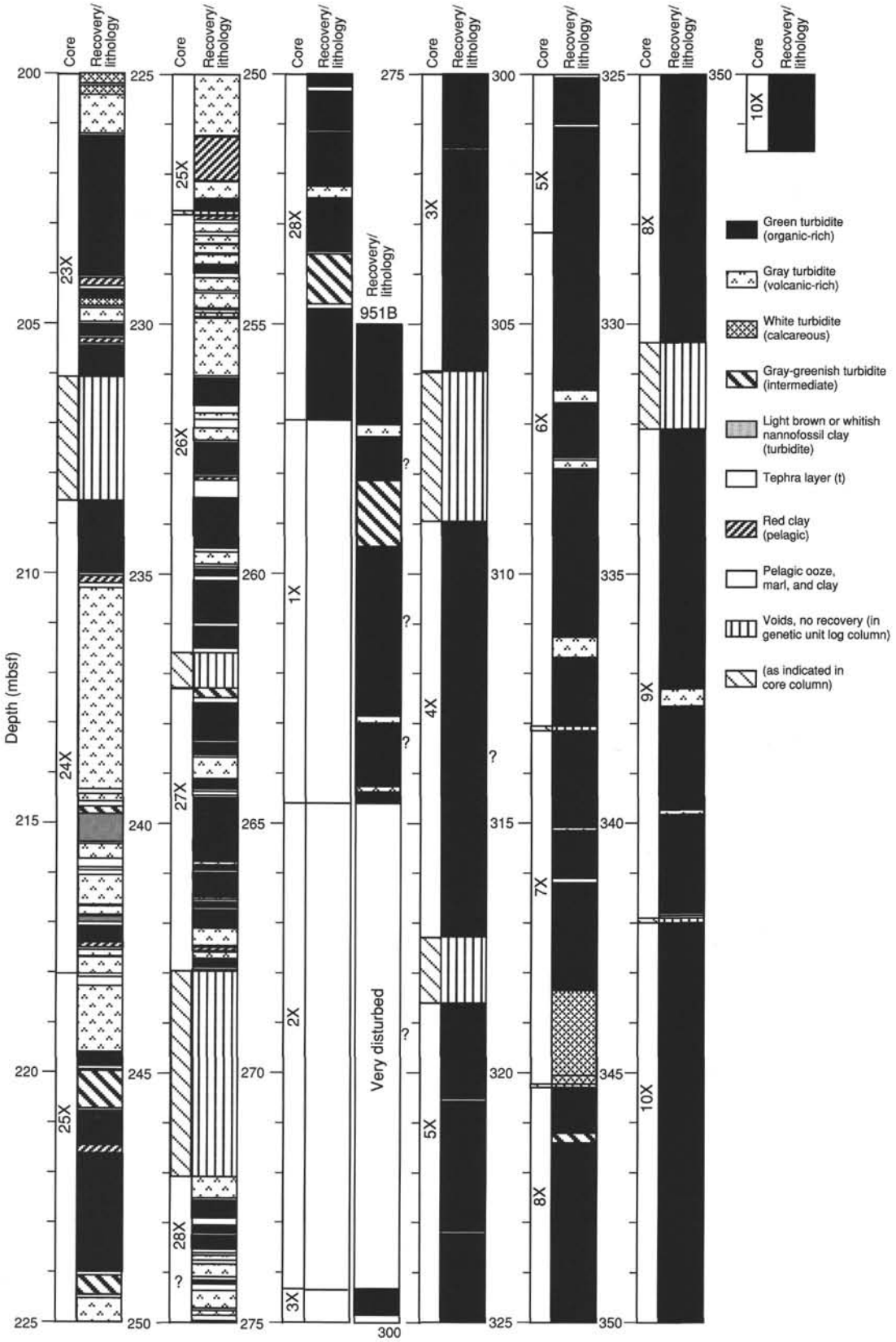

Figure 4 (continued).

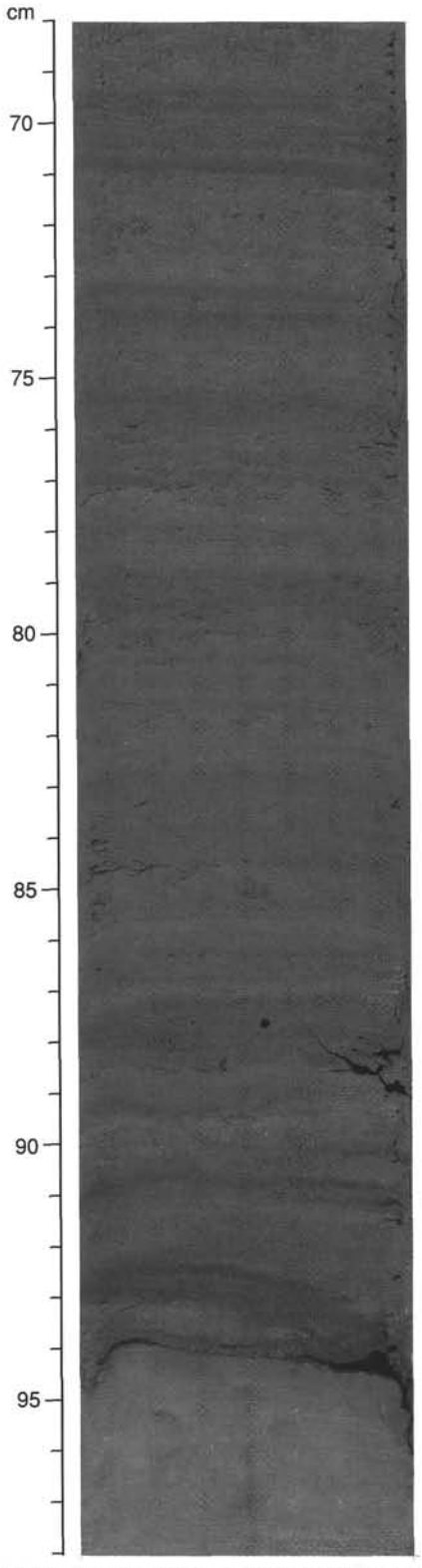

Figure 5. Silty base of an organic-rich turbidite showing parallel lamination. Note also the sharp lower contact with the underlying pelagic unit at 94 cm. Interval 157-951A-10H-4, 68–98 cm.

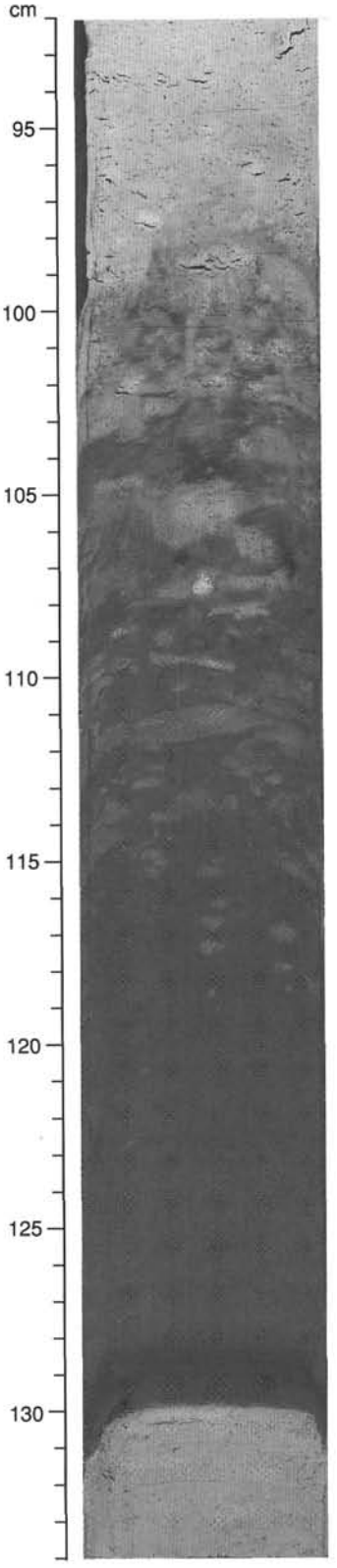

Figure 6. Gray, volcanic turbidite, illustrating the difference between the upper, gradational contact and the lower, sharp contact. Note also the extent of penetration of bioturbation from the overlying pelagic ooze. Interval 157-951A-7H-5, 92–134 cm.

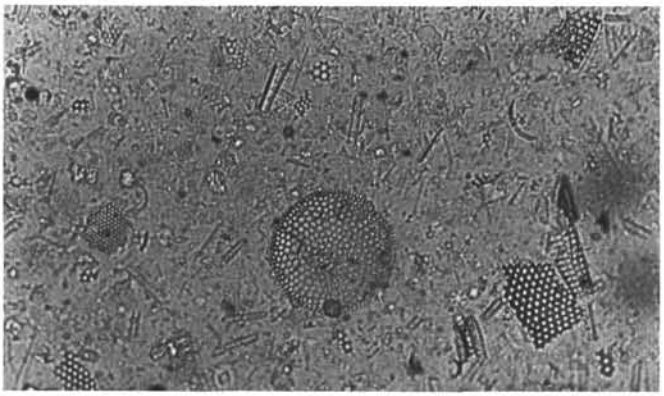

Figure 7. Photomicrograph of smear slide from the mud of an organic-rich turbidite showing common siliceous microfossils abundant through Hole 951B. Field of view is 0.6 mm wide. Sample 157-951A-3X, 3–9 cm.

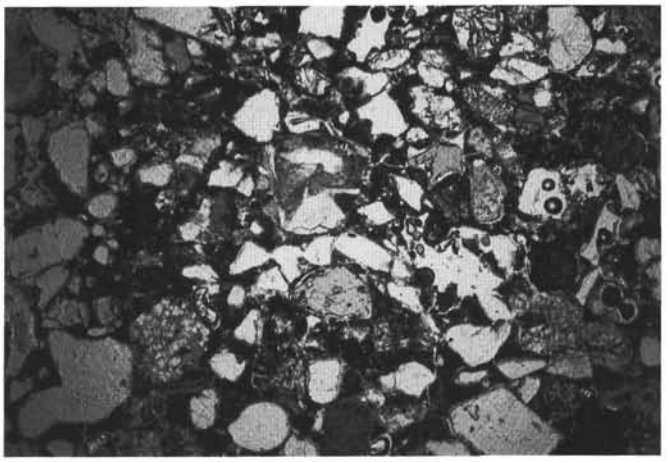

Figure 8. Photomicrograph of a smear slide from a 6.1-m-thick sandy base of a dark green turbidite consisting of quartz, feldspar, mica, pyroxene, amphibole, rutile, glauconite, carbonate particles, and glass shards. Field of view is 6.0 mm wide. Sample 157-951B-9X-3, 104–107 cm.

mbsf), contained the lowest occurrence of *G. oceanica*-like forms and marked the base of Zone CN14a. Also present in this sample is *Reticulofenestra asanoi,* which indicates that the sample belongs to the lowermost part of Zone CN14a. The highest occurrence of the large (>4 µm) *Gephyrocapsa* spp. interval is placed in Sample 157-951A-6H-4, 5 cm (47.35 mbsf); the highest occurrence of *Helicosphaera selli* is placed tentatively in Sample 157-951A-6H-4, 41.5 cm (47.72 mbsf), because *H. sellii* is rare at this site.

Pliocene

The highest commonoccurrence of *Discoaster brouweri* occurs in Sample 157-951A-8H-5, 45 cm (67.76 mbsf), marking the top of Zone CN12. Rare discoasters are present above this sample but are considered reworked. The lowest occurrence of common *D. triradiatus* occurs in Sample 157-951A-8H-6, 81 cm (69.61 mbsf), and indicates the upper part of Zone CN12d. The highest consistently occurring *D. pentaradiatus* is in Sample 157-951A-9H-6, 62 cm (79.42 mbsf), and marks the top of Zone CN12c. The top of Zone CN12b is indicated by the presence of *D. surculus* in Sample 157-951A-10H-5, 37 cm (87.17 mbsf), and the top of Zone CN12a in Sample 157-951A-11H-4, 148 cm (96.28 mbsf), by the highest occurrence of *D. tamalis.*

The highest consistently occurring *Reticulofenestra pseudoumbilicus* and *Sphenolithus* spp. are interpreted as Zone CN11b in Sample 157-951A-15X-CC, 5 cm (132.21 mbsf). Rare specimens of *R. pseudoumbilicus* are present above this level but are considered reworked. The lowest occurrence of *D. tamalis* in Sample 157-951A-16X-2, 53.5 cm (133.24 mbsf), indicates the base of Zone CN11b. The highest occurrence of *Amaurolithus* spp. in Sample 157-951A-17X-6, 60 cm (148.90 mbsf), marks the top of Zone CN10d. The lowest occurrence of *D. asymmetricus* in Sample 157-951A-19X-2, 119 cm (162.79 mbsf), marks the base of Zone CN10d. The section from Sample 157-951A-19X-6, 3 cm (167.63 mbsf), to Sample 157-951A-21X-6, 29.5 cm (187.20 mbsf), is only broadly defined as Zones CN10a to CN10c because *Ceratolithus* marker species were not seen in this interval.

Miocene

The presence of *Discoaster quinqueramus* in Sample 157-951A-21X-CC, 1 cm (188.83 mbsf), the marker for the top of Zone CN9b, indicates a late Miocene age. The highest occurrence of *A. amplificus,* which has a short range within Zone CN9b, occurs in Sample 157-951A-23X-5, 49 cm (205.19 mbsf). The lowest occurrence of *Amaurolithus* spp. (including *A. amplificus*) occurs in Sample 157-951A-24X-6, 102 cm (216.92 mbsf), below which all sampled pelagic sediments were barren of nannofossils except for one: Sample 157-951A-26X-1, 127 cm (228.97 mbsf), which contains a low abundance, low diversity assemblage with a single poorly preserved specimen of *Discoaster berggreni,* and so is tentatively assigned to Zone CN9.

Turbidites were sampled from Sample 157-951A-25X-6, 87 cm, to Sample 157-951B-10X-CC, 23 cm (351.13 mbsf), near the base of the hole. The youngest FO in all of these samples was that of *Reticulofenestra pseudoumbilicus* (specimens larger than 7 µm). This event is gradational and diachronous; however, as it occurs near the base of Zone CN5 (Young et al., 1994), none of the samples can be older than this. Therefore, the turbidite samples are assigned to Zones CN5–CN9 undifferentiated. Early Miocene, Paleogene, and Cretaceous species are present in the turbidites, although only early Miocene species such as *Sphenolithus heteromorphus* and *Helicosphaera ampliaperta* are common.

Planktonic Foraminifers

Planktonic foraminifers are abundant and well preserved in hemipelagic marls and oozes in the upper sequence of Hole 951A from Sample 157-951A-1H-2, 139–141 cm, to Sample 157-951A-9H-6, 62–64 cm (79.42 mbsf), but foraminifers are rare in the gray and calcareous turbidites from the same interval (Table 3). Both hemipelagic intervals and bases of turbiditic units below Sample 157-951A-10H-5, 32–34 cm (87.11 mbsf), are barren in Hole 951A. The turbidite bases at this locale are very fine grained, and unlike the calcareous turbidites of Site 950 they do not contain sand-size planktonic foraminifers. Only one sample bears foraminifers in Hole 951B, Sample 157-951B-7X-CC, 15–17 cm, from the sand-rich base of a calcareous turbidite. Samples 157-951B-1X-1, 87–89 cm, and 157-951B-3X-3, 49–51 cm, which were from sandy turbidite units, are barren of foraminifers.

Zones with good resolution are defined in the interval of hemipelagic marls and oozes from 2.89 to 79.42 mbsf in Hole 951A. The base of Zone N23 lies between 28.58 and 38.36 mbsf, based on the lowest occurrence of *Globigerina calida calida.* The base of Zone N22 lies between Samples 157-951A-8H-5, 52–54 cm, and 157-951A-8H-6, 75–77 cm, based on the lowest occurrence of *Globorotalia truncatulinoides.* The first appearance of this species also defines the base of the Pleistocene. The Pleistocene community contains abundant cool subtropical species including *Globorotalia*

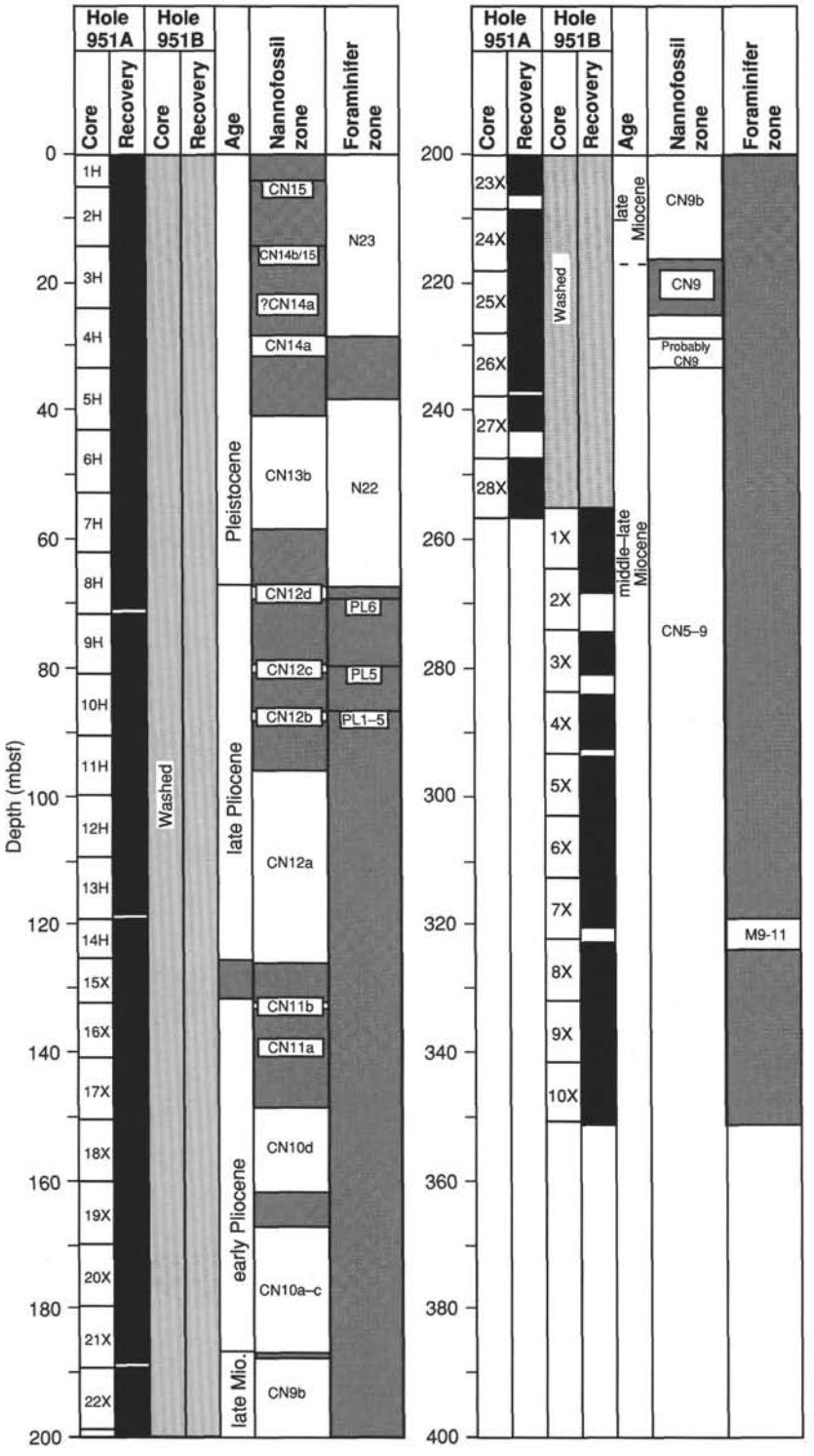

Figure 9. Nannofossil and foraminifer zonation at Site 951.

inflata and dextral *Neogloboquadrina pachyderma* and also few to common tropical species like dextral menardine globorotalid taxa (few *Globorotalia menardii cultrata* and *G. menardii menardii*), and common *Pulleniatina obliquiloculata obliquiloculata* and *P. finalis.*

Three samples contain late Pliocene zones. Sample 157-951A-8H-6, 75–77 cm, is assigned to Zone PL6 based on the presence of *Globorotalia inflata* and *Pulleniatina* without *Globorotalia mioceni-ca,* the last appearance of which defines the base of the zone. Sample 157-951A-9H-6, 62–64 cm, belongs in Zone PL5 based on the presence of *Globorotalia puncticulata* and the absence of *Pulleniatina* and *Globorotalia inflata,* which occur in overlying Zone PL6, and the absence of *Globoquadrina altispira,* the last appearance of which marks the base of Zone PL5. Sample 157-951A-10H-5, 32–34 cm, contains few, moderately preserved specimens from the base of a cal-

Table 2. Abundance, preservation, and lithology of samples used in nannofossil zonation, Holes 951A and 951B.

Core, section, interval (cm)	Depth (mbsf)	Abundance	Preservation	Zone	Lithology
157-951A-					
1H-3, 119.5–119.5	4.20	VH	G	CN15	Hemipelagic clay
2H-6, 83–83	13.13	VH	M	CN15–14b	Hemipelagic marl
3H-7, 8–8	22.38	VH	G	CN14a?	Turbidite
4H-4, 18–18	28.48	VH	G	CN14a	Hemipelagic ooze
4H-6, 18–18	31.48	H	G	CN14a	Hemipelagic clay
5H-5, 72–72	40.02	VH	G	CN13b	Hemipelagic marl
5H-6, 84.5–84.5	41.65	VH	G	CN13b	Hemipelagic marl
6H-4, 5–5	47.35	M	M	CN13b	Hemipelagic clay
6H-4, 41.5–41.5	47.72	M	P	CN13b	Hemipelagic clay
7H-2, 51.5–51.5	54.32	VH	G	CN13b	Hemipelagic ooze
7H-5, 63–63	58.93	H	G	CN13b	Hemipelagic ooze
8H-5, 45.5–45.5	67.76	VH	G	CN12d	Hemipelagic ooze
8H-6, 81–81	69.61	VH	G	CN12d	Hemipelagic ooze
9H-6, 62–62	79.42	VH	G	CN12c	Hemipelagic ooze
9H-7, 7.5–7.5	80.38	VH	G	CN12c	Hemipelagic ooze
10H-5, 37–37	87.17	H	G	CN12b	Hemipelagic marl
10H-6, 16–16	88.46	H	G	CN12b	Hemipelagic ooze
11H-4, 148–148	96.28	VH	M	CN12a	Hemipelagic marl
11H-5, 36–36	96.66	VH	M	CN12a	Hemipelagic marl
12H-1, 72–72	100.52	H	M	CN12a	Hemipelagic marl
12H-CC, 25–25	108.46	H	M	CN12a	Hemipelagic clay
13X-5, 23.5–23.5	114.97	VH	M	CN12a	Hemipelagic clay
13X-5, 71.5–71.5	115.45	H	M	CN12a	Hemipelagic clay
14X-3, 39–39	122.19	M	P	CN12a	Hemipelagic clay
14X-4, 22–22	123.52	H	M	CN12a	Hemipelagic clay
15X-1, 119–119	126.19	VL	G	CN12a	Hemipelagic clay
15X-CC, 5–5	132.21	L	G	CN11b	Hemipelagic clay
16X-2, 53.5–53.5	133.24	M	M	CN11b	Hemipelagic clay
16X-5, 64–64	137.84	M	G	CN11a	Hemipelagic clay
17X-6, 60–60	148.90	H	G	CN10d	Hemipelagic clay
18X-1, 101–101	151.51	L	P	CN10d	Hemipelagic clay
18X-6, 7.5–7.5	158.08	H	G	CN10d	Turbidite?
18X-7, 4–4	159.54	L	M	CN10d	Hemipelagic clay
19X-2, 119–119	162.79	L	G	CN10d	Hemipelagic clay
19X-6, 3–3	167.63	L	M	CN10a–c	Hemipelagic clay
19X-6, 50–50	168.10	B		CN10a–c	Hemipelagic clay
20X-5, 70–70	176.50	M	G	CN10a–c	Hemipelagic clay
20X-6, 50.5–50.5	177.81	B		CN10a–c	Hemipelagic clay
20X-6, 110–110	178.40	B		CN10a–c	Hemipelagic clay
21X-6, 29.5–29.5	187.20	L	P	CN10a–c	Hemipelagic clay
21X-CC, 1–1	188.83	M	G	CN9b	Hemipelagic clay
22X-2, 122–122	191.82	B		CN9b	Hemipelagic clay
23X-5, 16–16	204.86	M	M	CN9b	Hemipelagic clay
23X-5, 49–49	205.19	M	M	CN9b	Hemipelagic clay
24X-2, 18.5–18.5	210.09	B		CN9b	Hemipelagic clay
24X-6, 102–102	216.92	L	P	CN9b	Hemipelagic clay
24X-CC, 17.5–17.5	217.58	VL	P	CN9	Hemipelagic clay
25X-5, 44.5–44.5	224.45	B		Barren	Hemipelagic clay
25X-6, 87–87	226.37	VL	P	CN9 or older	Turbidite
25X-CC, 27–27	227.75	VL	P	CN9 or older	Turbidite
26X-1, 127–127	228.97	VL	P	Probably CN9	Hemipelagic clay
26X-4, 106–106	233.26	B		Barren	Hemipelagic clay
26X-5, 77–77	234.47	VL	P	CN5 to CN9	Hemipelagic clay
26X-5, 132–132	235.02	B		Barren	Hemipelagic clay
27X-3, 65–65	240.95	VL	P	No older than CN5	Hemipelagic clay
27X-CC, 44–44	242.68	VL	P	No older than CN5	Hemipelagic clay
28X-2, 60–60	249.10	VL	P	No older than CN5	Hemipelagic clay
28X-2, 122–122	249.72	H	M	No older than CN5	Turbidite
28X-4, 73–73	252.23	B		Barren	Hemipelagic clay
28X-4, 91–91	252.41	VH	M	No older than CN5	Turbidite
157-951B-					
1X-2, 52.5–52.5	257.03	B		Barren	Hemipelagic clay
1X-6, 68.5–68.5	263.19	VL	G	No older than CN5	Hemipelagic clay
1X-7, 4–4	264.04	B		Barren	Hemipelagic clay
3X-5, 30–30	276.47	B		Barren	Hemipelagic clay
3X-5, 31–31	280.61	B		Barren	Hemipelagic clay
4X-2, 24.5–24.5	285.65	B		Barren	Hemipelagic clay
4X-2, 66–66	286.06	B		Barren	Hemipelagic clay
4X-4, 75–75	289.15	VL	P	No older than CN5	Hemipelagic clay
5X-1, 128–128	293.88	L	P	No older than CN5	Hemipelagic clay
5X-CC, 39–39	303.49	L	M	No older than CN5	Hemipelagic clay
6X-2, 24–24	304.94	H	M	No older than CN5	Turbidite
6X-3, 115–115	307.35	H	M	No older than CN5	Turbidite
6X-6, 95–95	311.65	H	M	No older than CN5	Turbidite
7X-4, 90–90	318.30	H	P	No older than CN5	Turbidite
7X-5, 59–59	319.49	M	P	No older than CN5	Turbidite
8X-3, 18–18	325.68	H	M	No older than CN5	Turbidite
8X-4, 42.5–42.5	327.43	VL	P	No older than CN5	Turbidite
9X-5, 116–116	339.26	H	M	No older than CN5	Turbidite
10X-2, 55–55	343.95	B		Barren	Hemipelagic clay
10X-CC, 23–23	351.13	H	M	No older than CN5	Turbidite

Note: Key to abbreviations for abundance and preservation in "Explanatory Notes" (this volume).

Table 3. Abundance, preservation, and lithology of samples used in foraminifer zonation, Holes 951A and 951B.

Core, section, interval (cm)	Depth (mbsf) Top	Bottom	Abundance	Preservation	Zone	Lithology
157-951A-						
1H-2, 139–141	2.88	2.90	A	M	N23	Hemipelagic marl
2H-5, 91–93	11.70	11.72	F	P	N23	Gray turbidite
3H-5, 46–48	20.75	20.77	A	G	N23	Hemipelagic ooze
4H-4, 28–30	28.57	28.59	A	M	N23	Hemipelagic ooze
5H-4, 56–58	38.35	38.37	A	M	N22	Hemipelagic ooze
6H-2, 52–54	44.81	44.83	A	G	N22	Hemipelagic ooze
7H-5, 73–75	59.02	59.04	A	G	N22	Hemipelagic ooze
8H-5, 52–54	67.81	67.83	A	M	N22	Hemipelagic ooze
8H-6, 75–77	69.54	69.56	A	G	PL6	Hemipelagic ooze
9H-6, 62–64	79.41	79.43	A	P	PL5	Hemipelagic ooze
10H-5, 32–34	87.11	87.13	F	M	PL5 PL1	Calcareous turbidite
157-951B-						
1X-1, 87–89	255.86	255.88	B		?	Gray turbidite
3X-3, 49–51	274.78	274.80	B		?	Turbidite
7X-CC, 15–17	320.05	320.07	F	P	M9/M11	Calcareous turbidite

Note: Key to abbreviations for abundance and preservation in "Explanatory Notes" (this volume).

careous turbidite. Only five species were identified, and four of these range into the Miocene. The presence of *Globorotalia puncticulata* limits the sample to Zones PL5 to PL1, the total range of that species.

Sample 157-951B-7X-CC, 15–17 cm, from the sand-rich base of a distinctive calcareous turbidite in Hole 951B, is probably late to middle Miocene. The sample is heavily recrystallized so that many fossils are coated with calcareous cement and small calcite protuberances. The sample contains *Globigerinoides trilobus, Globoquadrina dehiscens, Globigerina nepenthes, Globorotalia* cf. *lenguaensis* and *Neogloboquadrina* cf. *continuosa* without *Nq. acostaensis* and is assigned to Zones M11 to M9. The turbidite probably correlates to another found in Core 157-950A-34X.

PALEOMAGNETISM

Introduction

Paleomagnetic measurements were made on the APC cores recovered from Hole 951A. They were demagnetized to at least 25 mT and analyzed for magnetostratigraphy. The results showed a bias toward normal polarity, as did the Hole 950A results, which was again interpreted as a normal overprint either acquired naturally, or by drilling, or both. The latter gave a component directed almost vertically downward, which was frequently removed by low demagnetization fields of between 5 to 10 mT. The inclination data were used as the primary indicator of polarity because the declination data are still puzzling, showing a common bias toward directions near the positive *x*-direction of the cryogenic magnetometer in uncorrected coordinates.

Most of the XCB cores from Hole 951A were measured in the long-core mode on the 2G magnetometer after demagnetization to 25 mT. The results show a stronger bias to normal polarity than the APC cores and appear to have acquired a stronger drill component, which was again directed vertically downward. The XCB data have not yet been analyzed for magnetostratigraphy because of the difficulty caused by the drill effects. Some of the XCB cores from Hole 951B were measured in the long-core mode, but measurements were stopped because of the low intensity of magnetization and the almost total domination of turbidites in the section. Moreover, biscuiting, combined with inflow of material between biscuits, makes interpretation of long-core measurements unreliable.

Discrete samples from APC and XCB cores were measured. They were compared with the whole-core measurement for quality control. We used primarily the gray turbidites and the pelagic interbeds, which are the most strongly magnetized material. In addition to standard analysis by Zijderveld plots and Schmidt nets, the NRM, ARM, and IRM characteristics were utilized in an attempt to discriminate reliable primary DRM and PDRM from remagnetized and drilling contaminated magnetizations.

A King diagram, which is a plot of ARM against initial susceptibility (k), was used to compare the magnetic behavior of different lithologies. Experiments attempted to clarify the puzzling preponderance of magnetization in the direction of the positive *x*-direction in the conventional ODP coordinates for the recovered core. Preliminary measurements of AMS on turbidites also were initiated.

Magnetostratigraphy

Plots of the inclination from all cores, the inclination from interbedded pelagics only, and interpreted chron boundaries are shown in Figure 10. The locations of the various chron boundaries are given in Table 4. Figure 11 shows the NRM intensity from the 2G Magnetometer and the susceptibility data from the APC whole-core MST measurements. The major peaks are again correlated to the gray (volcanic) turbidite layers, but some of the smaller are correlated to pelagic layers between green turbidites (e.g., 97 mbsf).

The inclination change recording the onset of the Brunhes was observed at 27 mbsf in Section 157-951A-4H-3, at 15 cm, in a brownish white marl. However, this is one of a number of thin pelagic interbeds within green and gray turbidites in this part of the core, which are too thin to give a reliable signal on the 2G in the continuous mode of measurement; the final resolution of this must await shore-based work with discrete samples. A transition in declination is seen as well.

The transition to normal inclination at the top of C1r.1n (Jaramillo) is seen in an interbedded clay between 31 and 32 mbsf, in interval 157-951A-4H-5, 125–135 cm, within green turbidites above and gray turbidites below. The inclination transition at the bottom of C1r.1n is found between 34 and 35 mbsf in Section 157-951A-5H-1. Unfortunately, the pelagic interbed lies at the top of Core 157-951A-5H and is disturbed. A reversed magnetized pelagic interbed was found in Section 157-951A-5H-4, at 50 cm, which belongs again to the C1r.

The reversed interval from the Jaramillo to the Olduvai is again obscured by turbidites that carry normal magnetization, but the interbedded pelagics reveal a better reversed record. A sharp transition in inclination at the top of C2n (Olduvai) is seen in both the pelagics-only plot and the record from all samples. This falls in nannofossil ooze at 59 mbsf in Section 157-951A-7H-5 at 60 cm. The base of the Olduvai is defined by a normally magnetized marl in Core 157-951A-

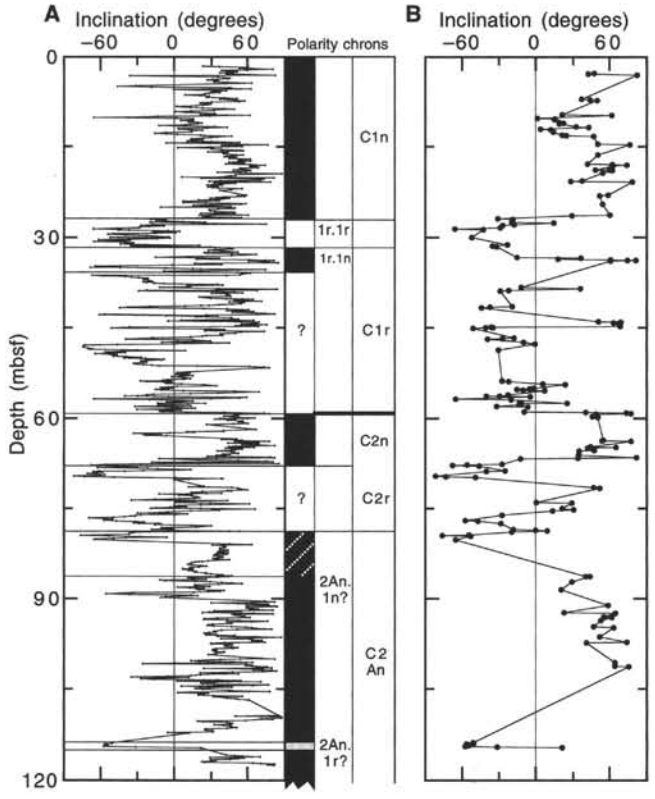

Figure 10. Magnetic data, NRM (25 mT), and interpreted polarity chrons from APC cores, Hole 951A. **A.** Inclination from all measurements. **B.** Inclination from measurements of pelagic interbeds. Filled areas = normal polarity, unfilled area = reversed polarity, shaded area = probable normal polarity, hatched area = probable reversed polarity.

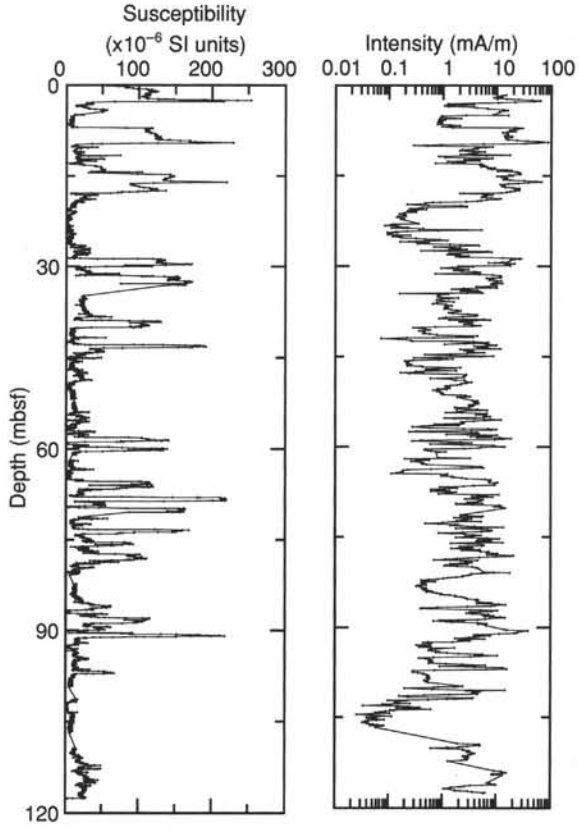

Figure 11. Susceptibility and intensity (NRM, 25 mT) from APC cores, Hole 951A.

Table 4. Polarity chrons: ages and correlated core intervals.

Boundary	Name	Age (Ma)	Reference	Depth (mbsf)	Core, section	Length (cm)
C1n (o)	Brunhes	0.78	SBP90	27.0	4H-3	15
C1r.1n (t)	Jaramillo	0.99	SBP90	31–32	4H-5	125–135
C1r.1n (o)	Jaramillo	1.07	SBP90	34–35	5H-1	0–60
C2n (t)	Olduvai	1.77	SBP90	59.0	7H-5	60
C2n (o)	Olduvai	1.95	SBP90	67.5	8H-4	90
C2An.1n (t)	Gauss	2.60	SBP90	80	10H-5	40
			H91	87	12H-1	15

Notes: (o) = onset, (t) = top. References as in "Explanatory Notes" (this volume).

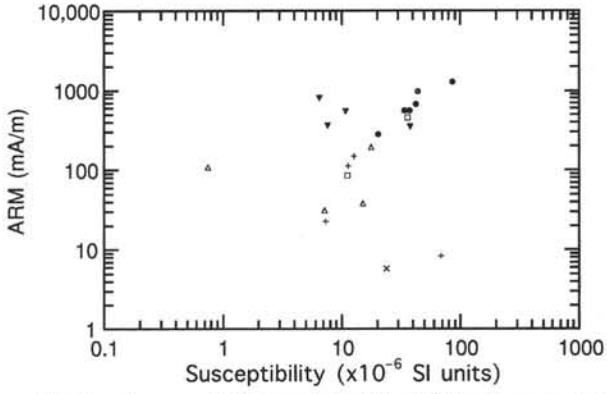

Figure 12. King diagram. ARM intensity (~100 mT, 0.1 mT) vs. weak field susceptibility. Filled circle = clay, open square = gray-green turbidite, + = gray turbidite, open triangle = nannofossil ooze, filled triangle = marl, and x = green turbidite.

8H at 66.4 mbsf, a marl of mixed polarity at 67 mbsf, and a reversed nannofossil ooze at 67.5 mbsf. The remainder of the Matuyama, C2r, is not clearly seen as a reversed interval even in the pelagics only plot. This may include a record of the Réunion Event.

The boundary between the base of the Matuyama and the Gauss C2An is difficult to establish and we can only restrict it to between 80 and 87 mbsf. However, C2r.1 is recorded as a clear reversed interval. The mixed polarities continue to the beginning of the Gauss and may include the Réunion Event.

Very few reversed directions are seen over an interval of nearly 25 m from 80 mbsf, which we interpret to be C2 An.1, the Gauss normal chron. There is a short reversed interval at 115 mbsf that we provisionally interpret as the Kaena. The magnetostratigraphy of the XCB cores has not yet been analyzed and will require further shore-based analyses.

Rock Magnetism

The demagnetization characteristics of NRM, ARM, and IRM, and measurements of weak field susceptibility were conducted as part of the preliminary rock magnetism analyses. The magnitudes of these parameters revealed systematic differences between the various lithologies. For example, in Figure 12 the intensity of ARM is plotted against weak field susceptibility (King Diagram) for a selection of lithologies. In such diagrams, if the grain size and magnetic material

is constant, but the amount varies, then the data points fall on a line, such as in clay samples from Hole 951A. The marls form a cluster to the left of the clay line indicating that they have predominantly finer grain magnetic material, and thus they should be excellent recorders.

Plots of NRM and ARM against IRM confirmed the long-core data. While the NRM of the turbidites gives poor Zijderveld plots and demagnetization characteristics unlike those of depositional remanence, some of the pelagics appear to be well behaved (Fig. 12). For example, Sample 157-951A-7H-4, 85 cm, appears to have acquired a very soft component, giving it an anomalously high ratio of NRM:IRM and high inclination (Fig. 13). However, after only 5 mT demagnetization it becomes shallow and the plot follows the ARM almost perfectly with a ratio of NRM:IRM of about 10^3, consistent with a DRM. The declination in this rock after orientation with the tensor tool is northerly and is consistent with its normal inclination. In contrast, Sample 157-951A-5H-6, 108 cm, has too high a ratio of NRM:IRM to be an ocean floor DRM, and therefore appears to be at least partially remagnetized.

A preponderance of declinations along the *x*-axis in uncorrected azimuth has been found in the Hole 951A archive cores, as it was in Hole 950A. From a practical viewpoint of establishing magnetostratigraphy, this drilling-induced magnetization is not a major problem in the APC cores from Leg 157 sites because we are at a sufficiently high latitude to use inclination.

Conclusions

The magnetostratigraphy of Hole 951A sediments has again been difficult to establish, but a preliminary magnetostratigraphy for the APCs has been generated that is consistent with that from Hole 950A and the proposed biostratigraphy at each site. It has become clear that where there are no significant pelagics, the magnetic record is unreliable in terms of magnetostratigraphy. Analysis of AF demagnetization of NRM has indicated that the pelagics carry an NRM that may be a primary DRM or pDRM, but the nature of the magnetization of the turbidites is not so clear.

INORGANIC GEOCHEMISTRY

Introduction and Operation

A total of 20 interstitial-water samples were taken at Site 951 between 2.95–336.50 mbsf (Table 5). The sampling strategy and analytical methods of Site 950 were continued at Site 951 (see "Explanatory Notes," this volume). Samples were analyzed for pH, salinity, chlorinity, alkalinity, sulfate, ammonia, sodium, potassium, silica, calcium, and magnesium. The bulk mineralogies of pore-water squeeze cakes and some additional samples were determined qualitatively by XRD analysis (Table 6).

Major changes in pore-water composition occur in response to biogeochemical reactions caused by the bacterially mediated oxidation of organic matter located principally in the organic-rich turbidites, and to diagenetic reactions in the silicate fraction, particularly the appearance of smectites and zeolites forming at the expense of volcanic glass in the lower part of the succession.

Chloride and Salinity

Salinity decreases from seawater values (35 g/kg) in the upper 30 m to a minimum of 32 g/kg around 150–250 mbsf. Chloride shows little depletion in this interval. Salinity increases to 33 g/kg below 270 mbsf.

Chloride fluctuates but is generally present at levels of around 560 mmol/L (close to the 559 mmol/L of seawater) in the upper 300 m of sediment, but it falls to 549 mmol/L toward the base of the hole. This

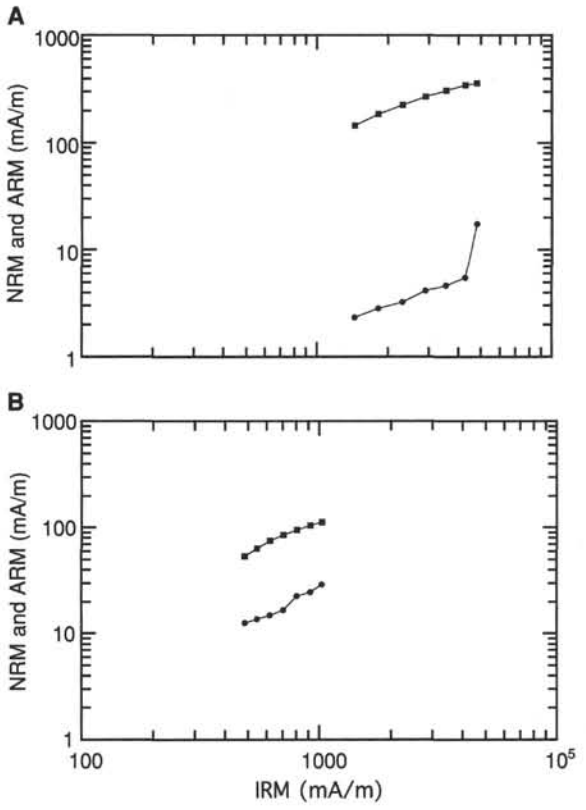

Figure 13. Demagnetization characteristics of NRM, ARM, and IRM. **A.** Sample 157-951-7H-4, 85 cm. **B.** Sample 157-951-5H-6, 108 cm. Filled circle = NRM, filled square = ARM.

Cl^- minimum, which is offset some distance below the salinity minimum, might result from the release of chemically bound water at depth from clays.

Sulfate and Alkalinity

The interstitial-water SO_4^{2-} profile (Fig. 14) shows progressive depletion from 27.6 mmol/L at 2.95 mbsf (slightly less than the typical seawater value of 28.9 mmol/L), to constant low values of 1–2 mmol/L between 195 mbsf and the bottom of the hole. This profile, typical of deep-water sequences undergoing sulfate reduction, shows a lower minimum compared to Site 950. The same arguments apply concerning sedimentation rates (again close to 3.4 cm/k.y.) being low enough to allow diffusional supply of sulfate to 200 mbsf at Site 951. Equilibrium is nearly reached between sulfate diffusion and sulfate consumption in the lower part of the hole, but very low residual values of SO_4^{2-}, combined with an absence of significant methane, indicate that sulfate reduction has not quite reached completion. Decreasing sulfate in the uppermost beds is matched by increasing alkalinity and ammonia production, as at Site 950.

Alkalinity increases from 3.43 mmol/L at 3 mbsf (slightly higher than the 2.3 mmol/L seawater value), to a maximum of 4.96 mmol/L around 20 mbsf (Fig. 14), then declines slowly to a minimum of 2.91 mmol/L around 155 mbsf, before increasing again slightly to 3.54 mmol/L at 195 mbsf. From 200 mbsf to the bottom of the core a strong increase in alkalinity is noticeable, with a maximum of 12.2 mmol/L. Increasing alkalinity in the upper beds may be attributed to H_2S and HCO_3^- production accompanying sulfate reduction. The location of the upper alkalinity maximum some distance above the sulfate minimum and the ammonia maximum may be explained by

Table 5. Interstitial-water geochemistry, Holes 951A and 951B.

Core, section, interval (cm)	Depth (mbsf)	pH	Salinity (g/kg)	Cl (mmol/L)	Alkalinity (mmol/L)	SO_4 (mmol/L)	NH_4 (µmol/L)	Na (mmol/L)	K (mmol/L)	SiO_2 (µmol/L)	Ca (mmol/L)	Mg (mmol/L)	Mg/Ca (molar ratio)
157-951A-													
1H-2, 145–150	2.95	7.58	35.0	557	3.43	27.6	103	466	11.3	285	10.3	51.7	5.02
2H-4, 145–150	10.75	7.58	35.0	562	4.93	25.9	274	467	10.6	285	9.65	49.5	5.13
3H-4, 145–150	20.25	7.43	35.0	561	4.96	23.7	331	471	11.0	591	9.53	48.5	5.08
4H-4, 145–150	29.75	7.53	35.0	562	4.36	21.5	451	485	11.0	492	9.30	49.1	5.28
5H-4, 145–150	39.25	7.51	34.0	559	4.51	21.1	468	499	10.5	427	8.57	48.3	5.63
6H-4, 145–150	48.75	7.58	34.0	561	4.15	18.3	587	481	10.0	294	7.59	44.2	5.82
7H-4, 145–150	58.25	7.74	34.0	561	3.55	16.3	664	473	9.50	236	6.24	43.6	6.99
8H-5, 145–150	68.75	7.56	33.0	557	3.26	14.0	704	468	9.31	238	5.80	41.3	7.12
9H-4, 145–150	77.25	7.67	33.0	561	3.49	13.0	811	479	8.98	184	6.57	40.4	6.15
10H-5, 145–150	88.25	7.52	33.0	555	3.42	11.4	977	493	8.80	211	7.22	39.4	5.45
14X-3, 145–150	123.25	7.62	33.0	559	3.42	7.39	1010	476	8.15	193	7.40	35.2	4.75
16X-4, 140–150	137.15	7.73	33.0	561	3.54	8.90	1050	482	7.99	202	7.86	34.5	4.39
18X-4, 140–150	156.40	7.48	32.0	562	2.91	4.80	1210	458	7.33	182	8.01	31.4	3.93
20X-4, 140–150	175.70	7.72	32.0	558	3.36	3.71	1200	474	7.41	245	8.77	31.6	3.61
22X-4, 140–150	195.00	7.58	32.0	561	3.54	1.75	1250	457	7.40	229	8.16	29.7	3.63
25X-4, 140–150	223.90	7.59	32.0	561	5.84	1.29	1090	451	6.35	256	8.81	31.1	3.53
28X-4, 140–150	252.90	7.85	32.0	562	8.27	3.93	1010	458	6.63	429	11.7	34.2	2.93
157-951B-													
3X-3, 140–150	278.70	6.98	33.0	562	11.2	0.91	1210	456	7.40	1170	13.9	31.0	2.23
6X-4, 140–150	309.10	7.70	33.0	558	12.2	2.10	1150	445	7.02	988	15.7	32.1	2.04
9X-3, 140–150	336.50	7.63	32.5	549	11.4	1.93	1140	452	6.28	1140	16.9	33.1	1.95

Table 6. Mineralogy of Site 951 sediments determined by XRD analysis.

Core, section, interval (cm)	Depth (mbsf)	Lithology	Mineralogy: Dominant minerals	Mineralogy: Accessory phases
157-951-A				
1H-2, 145–150	2.95	Ash layer	Volcanic glass	Calcite, feldspar, quartz
2H-4, 145–150	10.75	White turbidite	Calcite	Quartz
3H-4, 145–150	20.25	Green turbidite	Calcite, quartz	Clay minerals, dolomite
4H-4, 145–150	29.75	Gray turbidite	Calcite	Clay minerals, feldspar, quartz
5H-4, 145–150	39.25	Gray turbidite	Calcite	Clay minerals, feldspar, quartz
6H-4, 145–150	48.75	Pale gray/green turbidite	Calcite, quartz	Dolomite, feldspar, illite
7H-4, 145–150	58.25	Gray turbidite	Calcite	Feldspar, quartz
8H-5, 145–150	68.75	Hemipelagic ooze	Calcite	Quartz
9H-4, 145–150	77.25	Gray turbidite	Calcite	Feldspar, quartz
10H-5, 145–150	88.25	Gray turbidite	Calcite	Feldspar, quartz
14X-3, 145–150	123.25	Pale green turbidite	Calcite	Feldspar, quartz
16X-4, 145–150	137.15	Dark green turbidite	Calcite, quartz	Dolomite, kaolinite, smectites
17X-3, 33–34	144.13*	Gray/green turbidite	Calcite	Dolomite, feldspar, kaolinite, smectites, quartz
18X-4, 140–150	156.40	Gray turbidite	Calcite	Feldspar, quartz
18X-5, 69–70	157.19*	Green turbidite	Calcite	Dolomite, feldspar, illite, kaolinite, quartz
19X-4, 123–125	165.83*	Gray turbidite	Calcite	Feldspar, kaolinite, quartz, smectites
20X-2, 134–136	178.64*	Dark green turbidite	Quartz, smectites	Kaolinite
20X-4, 140–150	175.70	Light green turbidite	Calcite, quartz	Dolomite, illite, kaolinite
21X-5, 140–150	186.8*	Brownish green turbidite	Calcite, quartz	Dolomite, feldspar, illite, kaolinite, smectites
22X-4, 145–150	195.00	Light greenish gray turbidite	Quartz	Calcite, kaolinite, smectites
25X-4, 140–150	223.90	Gray turbidite	Calcite, quartz	Feldspar, kaolinite, smectites
28X-4, 140–150	252.90	Green turbidite	Calcite, quartz	Kaolinite, smectites
157-951B-				
1X-3, 47–49	258.47	Green turbidite	Calcite, quartz	Kaolinite, smectites
3X-3, 140–150	278.70	Green turbidite	Calcite, quartz, smectites	Phillipsite
4X-2, 30–32	285.7*	Green turbidite	Qartz, smectites	Calcite, feldspar
6X-4, 140–150	309.10	Green turbidite	Calcite, quartz	Kaolinite, smectites
6X-6, 69–71	311.39*	Gray turbidite	Calcite, feldspar, smectites	
9X-3, 140–150	336.50	Green turbidite	Calcite, quartz	Phillipsite, smectites
10X-4, 61–63	347.01*	Green turbidite	Quartz, smectites, phillipsite	

Note: All samples are pore-water squeeze cakes except those marked by an asterisk, which are additional material.

carbonate precipitation at and below 70 mbsf consuming alkalinity. The marked increase in alkalinity in the lower part of the section occurs around the lithological change to a carbonate-depleted, organic-rich turbidite dominated sequence (see Fig. 15), and may be caused by enhanced bacterial activity in this interval, possibly associated with an increased organic matter reactivity in these more siliceous sediments.

Ammonia

Ammonia increases progressively from 103 to 1250 µmol/L at ~195 mbsf (Fig. 14) and then remains high but variable below. A minimum value of 1010 µmol/L at 253 mbsf is coincident with an anomalously high sulfate value of 3.93 mmol/L that may be caused by contamination from drilling fluid. Some of the variation in the lower beds may be a result of NH_4^+ reactions with clay minerals. Ammonia and sulfate show essentially opposing trends, confirming that the former is being generated largely by sulfate reduction of organic matter in the turbidites.

Calcium and Magnesium

Calcium decreases from close to seawater values of 10.3 mmol/L (Fig. 15) at 3 mbsf to a marked minimum of 5.80 mmol/L at 70 mbsf, indicating Ca^{2+} uptake into the solid phase at that level. Below this,

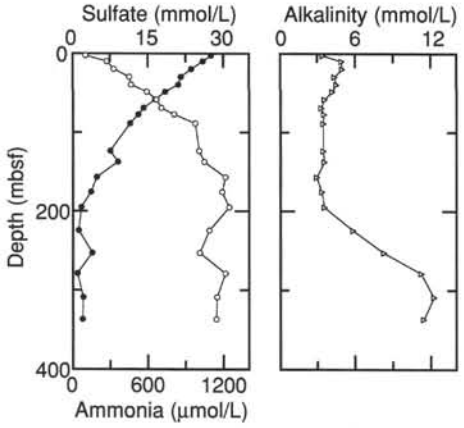

Figure 14. Pore-water sulfate (filled circles), ammonia (open circles), and alkalinity at Site 951.

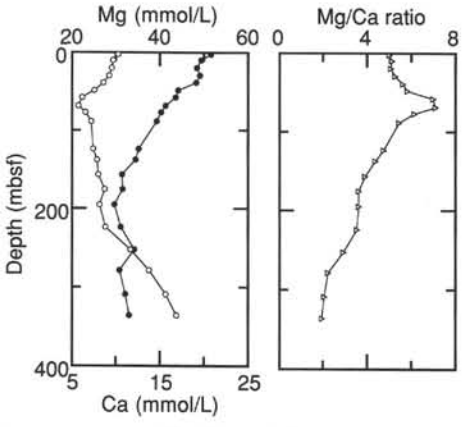

Figure 15. Pore-water magnesium (filled circles), calcium (open circles), and Mg/Ca ratio at Site 951.

concentrations rise again steadily before rising sharply below 200 mbsf, producing a maximum of 17 mmol/L in the bottom sample. The Ca^{2+} minimum lies below the upper alkalinity maximum, which is consistent with carbonate precipitation consuming bicarbonate. The bottom sample taken at Site 951 contains only half the Ca^{2+} concentration compared with the same depth at Site 950, indicating lower rates of calcium solubilization from the solid phase.

By contrast, Mg^{2+} generally declines in the pore waters, from near-seawater values of 51.7 mmol/L near the surface (Fig. 15) to a minimum of 30 mmol/L around 200 mbsf. The lowest beds display variable but marginally higher Mg^{2+} concentrations. The Mg/Ca ratio peaks at the Ca^{2+} minimum, indicating that sulfate reduction and alkalinity production are promoting calcite precipitation in the upper 70 m, below which dolomite precipitation and calcite dissolution occurs.

Dolomite, a more common diagenetic phase (Table 6), could be precipitating through much of the sequence. However, the rate of the reaction must decrease significantly below 300 mbsf, where the Mg/Ca ratio falls to <2. Low pore-water Mg^{2+} below 150 mbsf and associated Ca^{2+} production may additionally result from diagenetic reactions within the silicate fraction, probably controlled by the formation of smectites.

Shifts in the pore-water profiles of the alkali earths correspond to major changes in the carbonate content of the sediment, with the disappearance of high-carbonate pelagic sediments around 70 mbsf and a major decline in the carbonate content of both organic-rich and volcanic turbidites below 220 mbsf. Such changes should affect pore-water carbonate equilibria, although the precise relationships are currently unclear.

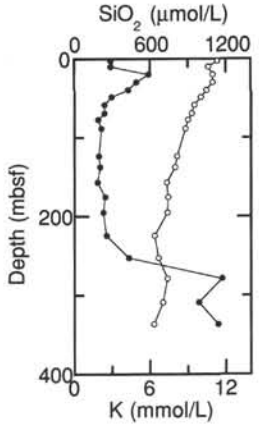

Figure 16. Pore-water silica (filled circles) and potassium (open circles) at Site 951.

Silica

Silica, a sensitive indicator of lithological change, climbs sharply from surficial values of 290 µmol/L (within a volcanic glass-rich level at 3 mbsf, Table 6) to a maximum of 590 µmol/L at 20 mbsf (Fig. 16), before steadily declining to a minimum of 180 µmol/L at 80 mbsf. Between 80 and 160 mbsf silica fluctuates around 200 µmol/L. The silica maximum at 20 mbsf, which occurs within a 7-m-thick package of organic-rich turbidites, is probably caused by the dissolution of biogenic opal; diatoms occur as a minor component of these turbidites in the shallower part of the sequence, but temporarily disappear around the silica pore-water maximum. Although this silica maximum is some 10 m shallower at Site 951 than at Site 950, it occurs in correlative sediment packages, the depth difference being attributable to several meters of missing sediment in the upper part of Hole 951A.

Declining silica concentrations below 20 mbsf with values down to 180 µmol/L indicate uptake of silica by the precipitation of diagenetic phases, principally smectites (Table 6). High values of up to 1170 µmol/L below 260 mbsf are associated with the renewed occurrence of biogenic silica (diatoms) in the section, as well as higher contents of smectites and phillipsite in the basal beds of the hole.

Potassium

Pore-water potassium concentrations (Fig. 16) decline from those slightly higher than seawater values of around 11 to 6.28 mmol/L in the deepest sample.

ORGANIC GEOCHEMISTRY

The shipboard organic geochemistry program at Site 951 followed the same procedures used for Site 950 (see "Organic Geochemistry" section of the "Site 950" chapter, this volume).

Volatile Hydrocarbons

Concentrations of methane (C_1) and ethane (C_2) gases were monitored in every core using the standard ODP headspace-sampling technique as part of the SSP program. The methane content remained

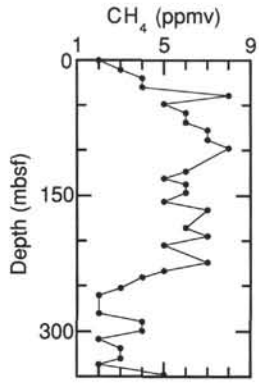

Figure 17. Methane concentrations in headspace samples from Site 951.

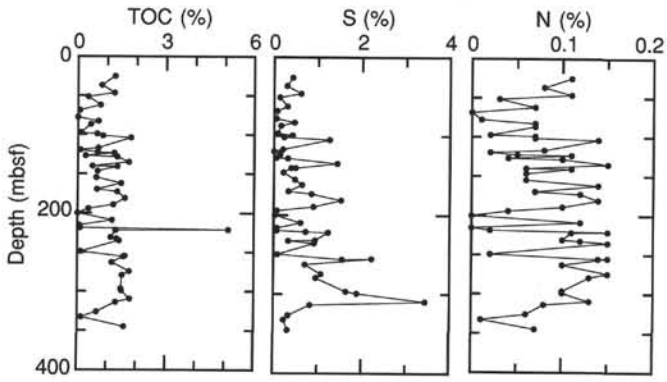

Figure 18. Concentration profiles of TOC, total sulfur, and total nitrogen at Site 951.

constantly low (2–8 ppmv; Fig. 17) throughout the entire sediment sequence of Site 951. No ethane was detected.

Carbon, Nitrogen, and Sulfur Concentrations

Results for determinations of organic carbon, total carbon, total nitrogen, and total sulfur are presented in Figure 18 and Table 7. A total of 193 samples were analyzed for carbonate; results were plotted according to lithology (Fig. 3) in the same way as for Site 950 (see "Lithostratigraphy," this chapter). The calcium carbonate showed an almost identical variation with depth for the four different lithologies. The observed decline in carbonate contents of organic-rich turbidites between 200 and 250 mbsf is shown more distinctly in the results from Site 951 (Fig. 3). Suitable carbonate samples were analyzed for organic carbon, nitrogen, and sulfur.

The volcanic turbidites vary in organic carbon content from below detection to 0.4% C but with an anomalous high value, 1.31%, from the deepest sample at 222 mbsf (Table 7), and with no systematic variation with depth. Volcanic turbidites are scarce below 225 mbsf, which coincides with a sudden decrease in calcium carbonate content of the organic turbidites. Nitrogen and sulfur occur in low concentrations without any systematic variation.

In the organic, green to dark green, turbidites, organic carbon varies between 0.5% and 1.8% in 53 samples down to 345 mbsf. Four samples show lower values, and 25 samples have values above 1.0% organic carbon. One sample (157-951A-25X-3, 32–33 cm) gave repeated results of 5.1% organic carbon, but contamination seems likely, as this value departs significantly from the general trend. Nitrogen values in the same samples varied between 0.07% and 0.15% in the organic turbidites with no apparent systematic trend. Sulfur content generally varied between 0.1% and 3.3% (Table 7 and Fig. 18).

Organic carbon and sulfur appear to increase slightly with depth in the organic turbidites. Nitrogen shows no systematic variation trends, but it follows individual values of increased and decreased organic carbon and sulfur (Fig. 18). Sulfur has a strong maximum at 310 mbsf coinciding with moderate highs in organic carbon and nitrogen. This is followed by a simultaneous decrease in the three components between 313–335 mbsf, perhaps because the turbidites in the deepest parts are more numerous and are thinner, leading to an overall increased proportion of oxidized sediment in the section. C/N ratios for the organic turbidites generally vary between 8 and 23, with the majority being 10 and 15, which probably indicates a predominance of marine-derived organic matter.

PHYSICAL PROPERTIES

Introduction

Measured physical properties included nondestructive GRAPE bulk density, magnetic susceptibility, and *P*-wave velocity from whole-round core sections using the MST, as well as thermal conductivity following the full-needle probe method. Shear strength, longitudinal *P*-wave velocity, and index properties were measured from split sections or discrete samples (see "Explanatory Notes," this volume). Core disturbance notably increased on XCB cores, which affected the measurement of some physical properties. In general, physical properties variations for Site 951 define intervals that agree closely with the lithostratigraphic units (see "Lithostratigraphy," this chapter) or that indicate compositional changes within the sediment.

Whole-core Measurements

MST

Whole-round measurements of GRAPE density and magnetic susceptibility were made on all cores from Holes 951A and 951B. Void spaces between sediment core and the plastic liner impeded measurement of *P*-wave velocity on XCB cores below 118 mbsf. Before MST logging, cores were allowed to thermally equilibrate to room temperature for approximately 4 hr. Sampling rate was typically one measurement every 1.5 to 2 cm for the *P*-wave logger, 2.5 cm for the GRAPE, and 3 cm for magnetic susceptibility. Total natural gamma activity was not measured on Site 951 because of time constraints. For details on the MST sensors see the "Explanatory Notes" chapter of the Leg 156 *Initial Reports* volume. Data obtained from all three sensors are shown on Figures 19 through 27.

Magnetic Susceptibility

Volumetric magnetic susceptibility was measured in all cores recovered from Holes 951A and 951B, but the quality of the measurements degraded on core sections below 250 mbsf as a result of increased core disturbance. The volume magnetic susceptibility data for Holes 951A (0–257 mbsf) and 951B (255–352 mbsf) are plotted on Figures 19 and 20. In general, magnetic susceptibility trends downcore are generally useful for lithology interpretation and stratigraphic correlations between holes, and at Site 951 they have been especially useful for defining volcanic turbidite intervals. The magnetic susceptibility data for Hole 951A (Fig. 19) shows numerous high-amplitude spikes that are related to lithologic or compositional variations. High values above 110×10^{-6} SI units correlate with intervals of volcaniclastic turbidites that are much more common above 250 mbsf. Green and calcareous turbidites together with pelagic units show consistently low magnetic susceptibility values.

GRAPE Bulk Density

The GRAPE density data collected at Holes 951A and 951B are displayed in Figures 21 and 22. Filtered data points correspond to the average data value within a 0.125 m filter window. Although a large number of spikes are still present, they may actually correspond to

Table 7. Elemental and organic carbon compositions of sediments, Site 951.

Core, section, interval (cm)	Depth (mbsf)	Sediment type	Inorganic carbon (%)	$CaCO_3$ (%)	Total carbon (%)	TOC (%)	Total nitrogen (%)	Total sulfur (%)	C/N (ratio)
157-951A-									
4H-2, 22–23	25.52	O	5.88	49.0	7.14	1.26	0.11	0.41	11.5
5H-3, 38–39	36.68	O	5.77	48.1	6.57	0.80	0.08	0.29	10.0
6H-3, 51–52	46.31	O	5.48	45.6	6.71	1.23	0.11	0.60	11.2
6H-6, 100–101	51.30	V	8.47	70.6	8.82	0.35	0.03	0.13	11.7
8H-1, 55–56	62.35	O	5.88	49.0	6.63	0.75	0.07	0.30	10.7
8H-5, 108–109	68.38	V	7.31	60.9	7.36	0.05	BD	0.07	ND
9H-5, 58–59	77.88	V	7.57	63.1	7.38	0.00	0.01	0.05	ND
10H-2, 77–78	83.07	O	5.93	49.4	6.63	0.70	0.07	0.46	10.0
10H-4, 124–125	86.54	O	4.90	40.8	5.33	0.43	0.07	0.16	6.1
11H-5, 73–74	97.03	I	6.86	57.1	6.96	0.10	0.02	0.08	5.0
11H-6, 98–99	98.78	O	5.70	47.5	6.35	0.65	0.07	0.41	9.3
12H-2, 24–25	101.54	O	4.63	38.6	5.48	0.85	0.07	0.23	12.1
12H-4, 61–62	104.40	O	4.74	39.5	6.55	1.81	0.14	1.27	12.9
13H-6, 63–64	116.86	O	5.32	44.3	6.02	0.69	0.08	0.20	8.6
14X-1, 59–60	119.39	V	7.83	65.2	7.92	0.09	0.02	BD	4.5
14X-3, 122–123	123.02	O	8.07	67.2	8.73	0.66	0.05	0.14	13.2
14X-4, 100–101	124.30	O	6.59	54.9	7.83	1.24	0.11	0.13	11.3
15X-2, 62–63	127.12	V	5.97	49.7	6.24	0.27	0.04	0.06	6.8
15X-3, 39–40	128.39	O	1.05	8.7	2.40	1.35	0.10	0.32	13.5
16X-3, 85–86	135.05	O	3.61	30.1	5.35	1.74	0.15	1.44	11.6
16X-7, 18–19	140.38	O	5.02	41.8	5.51	0.49	0.06	0.49	8.2
17X-1, 17–18	140.97	O	1.90	15.8	3.26	1.36	0.11	0.38	12.4
17X-4, 106–107	146.36	O	4.64	38.7	5.31	0.67	0.06	0.21	11.2
18X-3, 129–130	154.79	O	5.33	44.4	5.95	0.62	0.06	0.47	10.3
19X-2, 56–57	162.16	O	4.37	36.4	5.84	1.47	0.14	0.64	10.5
19X-CC, 23–24	169.86	O	5.96	49.6	6.61	0.65	0.07	0.34	9.3
20X-3, 37–38	173.17	O	2.37	19.7	3.72	1.35	0.12	0.86	11.3
21X-2, 24–25	181.14	O	4.14	34.5	5.76	1.62	0.14	1.52	11.6
22X-1, 45–46	189.55	O	5.79	48.2	7.01	1.22	0.10	0.90	12.2
22X-4, 89–90	194.49	V	7.26	60.5	7.62	0.36	0.04	0.07	9.0
23X-2, 10–11	200.30	V	10.7	89.3	10.7	BD	BD	BD	20.0
24X-1, 98–99	209.38	O	3.95	32.9	5.13	1.18	0.12	0.61	9.8
24X-6, 32–33	216.22	V	4.72	39.3	4.78	0.06	BD	0.07	ND
25X-1, 117–118	219.17	V	7.93	66.1	8.00	0.07	0.02	0.07	3.5
25X-3, 32–33	221.32	O	0.40	3.3	5.52	5.12	0.15	0.73	34.1
25X-3, 122–123	222.22	V?	2.32	19.3	3.63	1.31	0.11	1.23	11.9
26X-3, 77–78	231.47	O	0.33	2.7	1.46	1.13	0.10	0.94	11.3
26X-4, 40–41	232.60	O	3.33	27.7	4.65	1.32	0.12	0.34	11.0
26X-6, 16–17	235.36	O	1.97	16.4	3.39	1.42	0.15	0.91	9.5
28X-2, 106–107	249.56	V	2.80	23.3	2.91	0.11	0.02	0.09	5.5
28X-6, 114–115	255.64	O	1.99	16.6	3.55	1.56	0.14	1.55	11.1
157-951B-									
1X-1, 48–49	255.48	O	1.99	16.6	3.61	1.62	0.15	2.22	10.8
1X-6, 39–40	262.89	O	4.07	33.9	5.25	1.18	0.10	0.71	11.8
3X-1, 33–34	274.63	O	1.30	10.8	3.05	1.75	0.15	1.07	11.7
3X-4, 94–95	279.74	O	2.15	17.9	3.68	1.53	0.13	0.96	11.8
5X-3, 11–12	296.71	O	0.89	7.4	2.37	1.48	0.10	1.64	14.8
5X-4, 132–133	299.42	O	1.14	9.5	2.63	1.49	0.10	1.89	14.9
6X-5, 58–59	309.78	O	1.22	10.2	3.01	1.79	0.13	3.44	13.8
7X-1, 84–85	313.74	O	2.54	21.2	3.85	1.31	0.08	0.83	16.4
8X-3, 99–100	326.49	O	1.24	10.3	1.89	0.65	0.06	0.34	10.8
9X-1, 42–43	332.52	O*	2.18	18.2	2.30	0.12	0.01	0.23	12
10X-3, 36–37	345.00	O	0.94	7.8	2.54	1.6	0.07	0.32	22.9

Note: I = intermediate turbidite, O = organic-rich turbidite, O* = oxidized turbidite top, V = volcanic turbidite.

fine-scale lithologic variations downcore. Along the entire profile, the larger peaks correspond to coarse-grained layers of either volcanic or calcareous turbidite intervals having densities between 1.8 to >2.0 g/cm^3, interbedded between the lower density (avg. 1.65–1.70 g/cm^3), organic-rich turbidites. The general trend of the average GRAPE density data shows a continuous increase downcore from values close to 1.50 g/cm^3 near the mud line to 1.82 g/cm^3 at about 120 mbsf, the lower limit of lithologic Subunit Ia (see "Lithostratigraphy," this chapter), where a sharp decrease in GRAPE density occurs. Below that depth the GRAPE density profile shows several segments with slight density increases downcore, separated by sharp decreases at 210, 265, and 325 mbsf, respectively. Some of the depth intervals with a sharp decrease in GRAPE density (at 120 and 210 mbsf) correlate well with decreases in carbonate content for the pelagic intervals, and for the volcanic and the organic-rich turbidites, respectively. Whereas some others may be related to changes on the chemical profile downcore (see "Inorganic Geochemistry," this chapter).

P-wave Velocity

P-wave velocity was measured at Hole 951A down to 118 mbsf. Filtered data are plotted against depth on Figure 23. Measured velocities are generally in the range between 1500–1575 m/s throughout the section with only small variations. These values are very close to the velocity of the water, which means that sediments of lithologic Subunit Ia have high water content. The average downcore profile shows a smooth sinusoidal pattern that results in a slight increase in velocity with depth.

Correlation of MST results

Data collected from all three sensors in Holes 950A and 950B are in Figures 39 through 42 of the "Site 950" chapter, this volume. These detailed plots confirm the presence of significant variations in physical properties at a relatively fine scale. There is a marked correlation between changes on some of the measured parameters and the

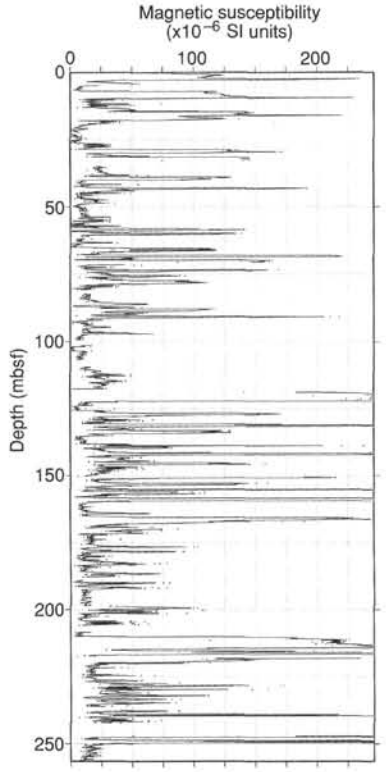

Figure 19. MST magnetic susceptibility, Hole 951A. Filtered data indicated by lines, raw data by discrete points.

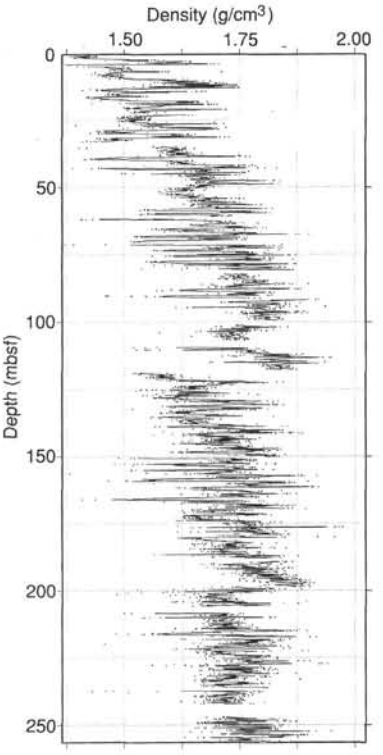

Figure 21. MST GRAPE density, Hole 951A. Filtered data indicated by lines, raw data by discrete points.

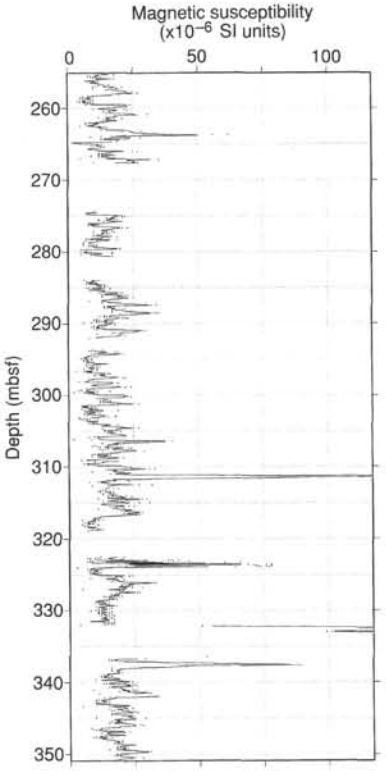

Figure 20. MST magnetic susceptibility, Hole 951B. Filtered data indicated by lines, raw data by discrete points.

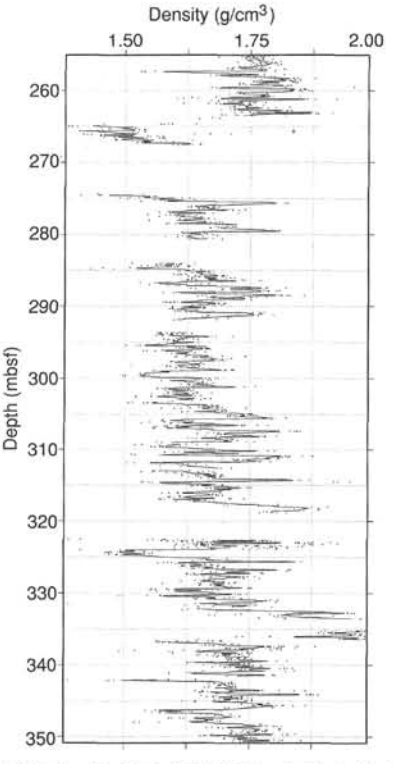

Figure 22. MST GRAPE density, Hole 951B. Filtered data indicated by lines, raw data by discrete points.

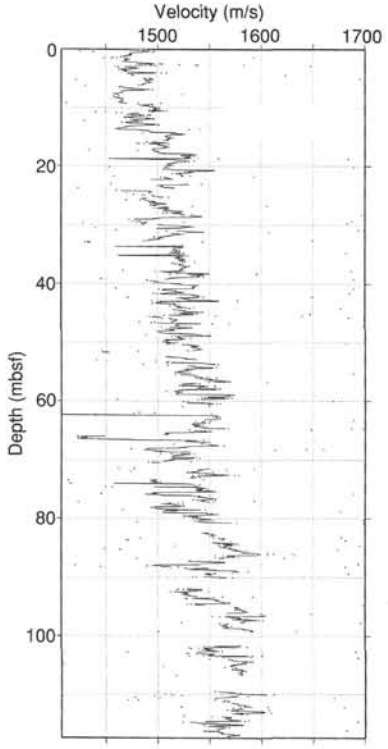

Figure 23. MST *P*-wave velocity, Hole 951A. Filtered data indicated by lines, raw data by discrete points.

different lithologies. Peaks of high magnetic susceptibility, in most cases corresponding to volcanic turbidites, are also characterized by relative lows in GRAPE density and *P*-wave velocity, whereas these two parameters show similar trends through all the measured core intervals. In general, volcanic turbidite levels are characterized by very high magnetic susceptibility, compared to the rest of sediment types, as well as by low density and velocity. In contrast, organic-rich turbidites show low magnetic susceptibility and high density and velocity. Calcareous- and intermediate turbidite-type intervals have typical properties between the organic and volcanic intervals.

Thermal Conductivity

Thermal conductivity measurements were routinely performed on the odd-numbered sections of each core. Needles were inserted 50 cm from the top of each measured section on all cores from Hole 951A, from the mud line to a depth of 250 mbsf. Drilling disturbance observed below 200 mbsf resulted in a lack of coherence or a large scattering of the measured thermal conductivity. This and the added difficulty of correctly inserting the probe within the more lithified sediments resulted in no thermal conductivity measurements on cores from Hole 951B. Thermal conductivity data are compiled in Table 8 and illustrated in Figure 28. A relatively large data scattering is observed through the hole, although there is a tendency for a slight increase of thermal conductivities downcore. This tendency for downcore increase seems to be interrupted at about 120 mbsf and 210 mbsf, where average measured values show either a relatively marked decrease or a change in the tendency downcore.

Discrete Measurements on Split Cores

Index Properties

Index properties, including wet- and dry-bulk density, water content, porosity, void ratio, and grain density were measured or calculated from weights and volumes of discrete samples, both in saturated and dry states. Sampling rate for index properties was approximately one per section in both holes of Site 951. Bulk density was calculated following Method B, and dry-bulk density, grain density, porosity, and void ratio were calculated using Method C (see "Explanatory Notes" and "Site 950," this volume). Values of the index properties for Site 951 are presented in Table 9 and are plotted on Figure 29.

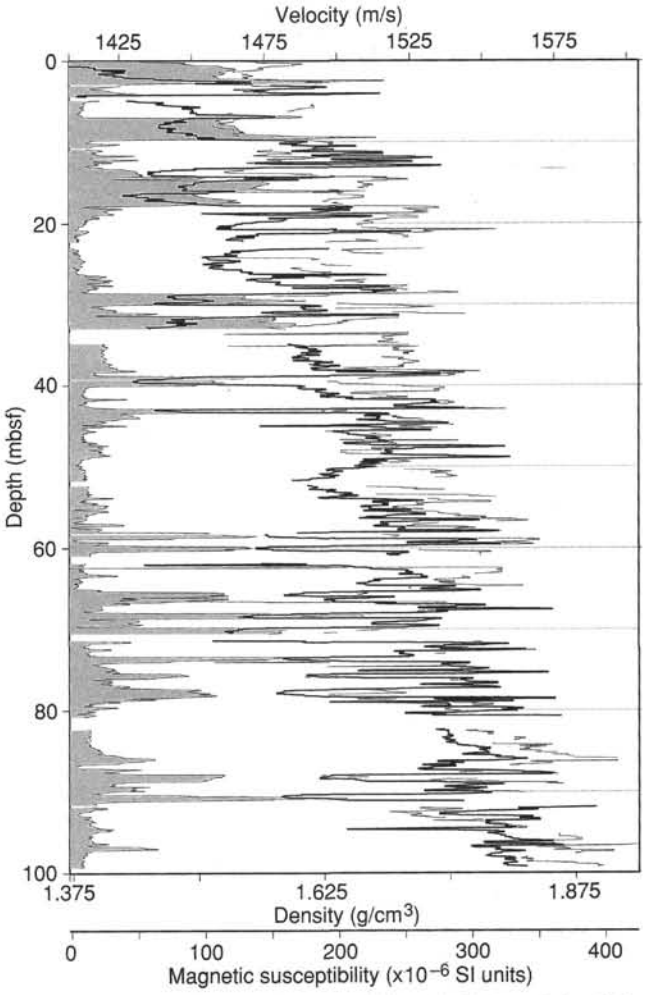

Figure 24. Filtered MST magnetic susceptibility (shading), velocity (light trace), and gamma-ray density (bold trace) for 0–100 mbsf, Hole 951A.

Lithologic Subunit Ia is characterized by a downcore increase of bulk and grain density as well as by a downcore decrease of water content and porosity down to 120 mbsf. At that depth, the boundary between lithologic Subunits Ia and Ib is marked by a relative increase in water content and porosity and by similar decreases in bulk and grain density. The upper part of lithologic Subunit Ib shows a similar pattern of physical properties trend downcore as Subunit Ia, but a major change occurs at about 210 mbsf where the downcore trend changes to a decrease in bulk and grain density and a downcore increase in water content and porosity, down to 300 mbsf. Notice that a major decrease in grain density occurs at about 260 mbsf (Fig. 29D). Below 300 mbsf, the lower part of Hole 951B shows a new change in the physical properties trend downcore, characterized by a net downcore increase of bulk and grain densities, and by a decrease in water content and porosity, although samples show a large scattering.

Along the entire hole, the highest bulk densities (from 1.85 to 2.08 g/cm^3, Fig. 29) correspond to the relatively coarse-grained base of some of the volcaniclastic turbidites or calcareous turbidite intervals.

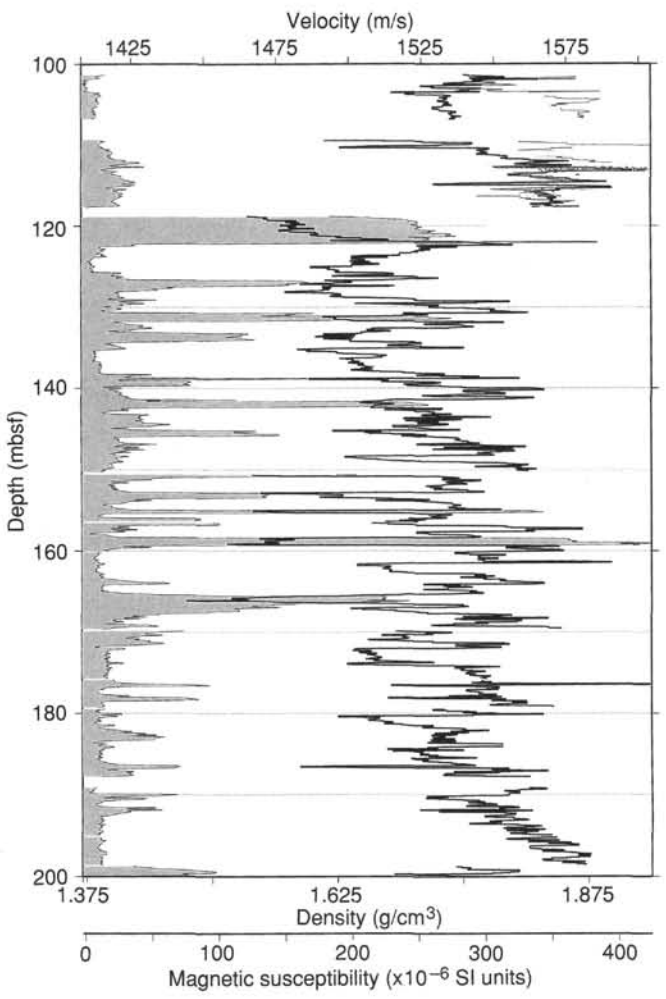

Figure 25. Filtered MST magnetic susceptibility (shading), velocity (light trace), and gamma-ray density (bold trace) for 100–200 mbsf, Hole 951A.

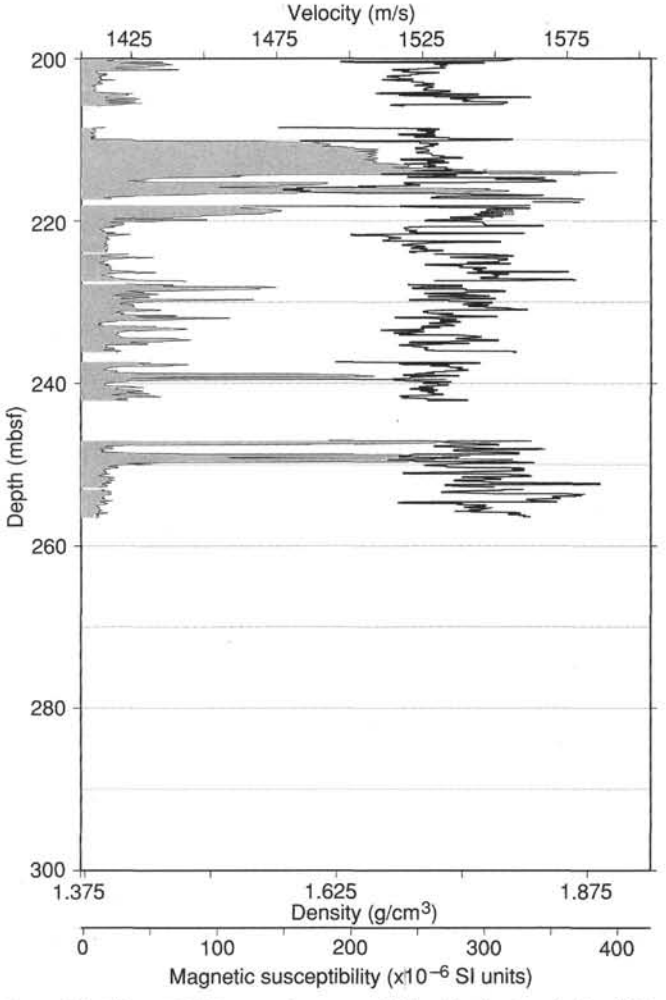

Figure 26. Filtered MST magnetic susceptibility (shading), velocity (light trace), and gamma-ray density (bold trace) for 200–300 mbsf, Hole 951A.

The larger measured values of grain density (Fig. 29) correspond to the silty and sandy intervals sampled from the bases of some turbidite beds.

Undrained Shear Strength

Undrained shear strength of the cored sediments was measured using the motorized vane shear or estimated using the handheld penetrometer. The vane shear device was used to a depth of 180 mbsf on Core 157-951A-21X, but the results showed a large scattering below 140 m as a result of the development of cracking within the sediments when tested. Vane shear values below 140 m should be accepted with caution. Below 40 mbsf sediment strength was also estimated with the handheld penetrometer, which was used until the sediment strength exceeded its measuring limits (approximately 250 kPa) at 260 mbsf. Both systems were used simultaneously for nearly 150 m of core. The comparison of the results obtained by the two systems gives a fairly good correlation, although penetrometer readings tend to give higher values than those obtained with the vane shear device. Data are presented in Table 10 and Figure 30.

The strength values increase downhole from very low values (near zero) on the seafloor to 220 kPa at about 200 mbsf. Both penetrometer and vane shear data show a large scattering below 120 mbsf. From 200 to 260 mbsf a slightly decreasing trend is observed for the shear strength, together with a relatively large scattering of the measured data. The data scattering may result from variations on sediment lithology and also from limitations of the method used, because some of the measured strengths are close to the limits of the system.

Discussion

The physical properties from Site 951 show a close relationship to the lithologic units and provide additional information to characterize sediment types within lithological subunits. Some of the measured physical properties (e.g., magnetic susceptibility) are especially useful for characterization of the volcanic turbidites. The index-property data, in general, are indicative of sediments undergoing progressive consolidation, but they are also indicative of changes in the chemical composition or texture of the sediment. The downcore increase of GRAPE density, thermal conductivity, compressional velocity, bulk density, and shear strength, as well as the downcore decrease of water content and porosity with depth, suggest that the dominant process within the upper 200 mbsf is gravitational compaction. In contrast, grain density, a parameter normally with a small variation and no general depth trend, shows downcore variations that result from changes in the chemical or mineralogical composition of the sediment. Variations in physical properties occur at about 120, 200, 250, and 300 mbsf, reflecting compositional changes within the sediment.

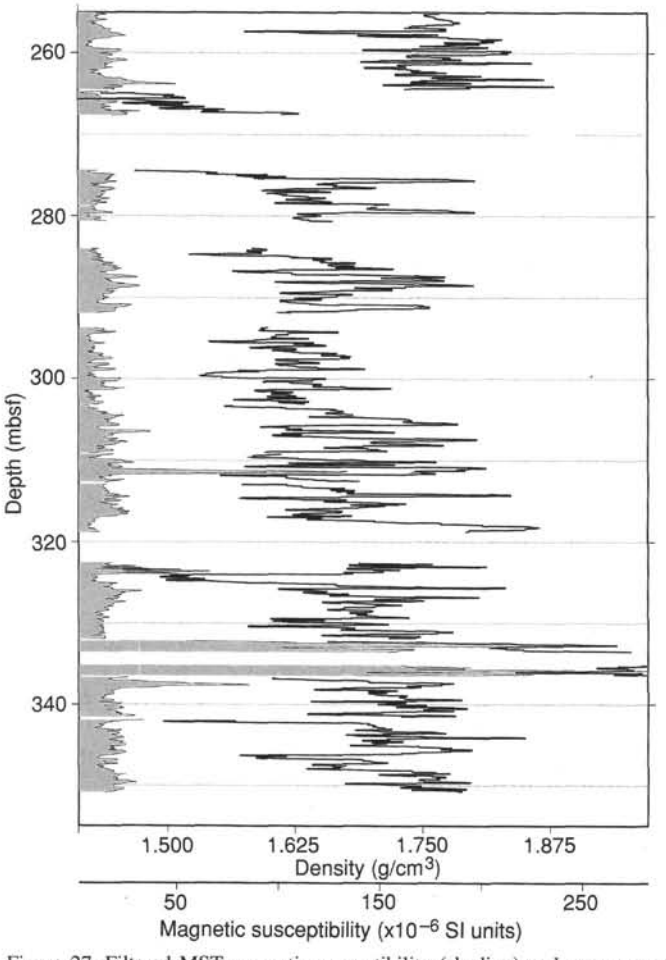

Figure 27. Filtered MST magnetic susceptibility (shading) and gamma-ray density (lines) for 255–350 mbsf, Hole 951B.

SEDIMENT ACCUMULATION RATES

Sediment accumulation rates for Site 951 are based on 18 nannofossil, 2 planktonic foraminiferal, and 5 paleomagnetic age determinations (Table 11). As at Site 950, most of the age data is concentrated in the upper part of the hole (0–217 mbsf) where calcium carbonate is better preserved in the pelagic layers. All datum levels were identified in pelagic layers except for the occurrence of *Reticulofenestra pseudoumbilicus* in the basal turbidite of Hole 951B.

Two types of sediment accumulation rate curves have been produced: one for the total sediment including turbidites and pelagic layers (Fig. 31), and one for the pelagic layers only (Fig. 32). The pelagics-only curve is based on the stacked thicknesses of pelagic clays, marls, and oozes and gives an indication of the background accumulation rate. Unfortunately, fewer datum levels were obtained in the deeper parts from this site than from Site 950, so the extrapolated rates for the interbedded clays are less well constrained than for Site 950.

Pelagic Accumulation Rates

The pelagic accumulation rates are well constrained by numerous data points in the upper 19 m of the stacked pelagic sequence (Fig. 31). The accumulation rate from zero to 2.6 Ma averages 4.4 m/m.y.

Table 8. Thermal conductivity measurements, Hole 951A.

Core, section, interval (cm)	Depth (mbsf)	Method	TCcorr (W/mK)	Standard error (W/mK)	Drift (°/min)
157-951A-					
1H-1, 50	0.50	F	0.830	8.48E-03	–0.010
1H-2, 50	2.00	F	0.940	1.42E-02	0.049
1H-3, 50	3.50	F	1.037	1.25E-02	0.051
2H-1, 50	5.30	F	1.198	9.33E-03	0.078
2H-2, 50	6.80	F	0.985	1.10E-02	–0.007
2H-3, 50	8.30	F	0.983	9.67E-03	0.021
2H-4, 50	9.80	F	1.265	1.30E-02	0.033
3H-1, 50	14.80	F	0.891	1.63E-02	–0.037
3H-3, 50	17.80	F	0.907	9.67E-03	–0.007
3H-5, 50	20.80	F	1.140	1.49E-02	0.016
5H-1, 50	33.80	F	1.036	5.94E-03	–0.024
5H-3, 50	36.80	F	0.957	8.33E-03	–0.049
5H-5, 50	39.80	F	0.937	1.53E-02	–0.002
5H-7, 50	42.80	F	1.065	8.17E-03	–0.035
6H-1, 50	43.30	F	0.912	1.12E-02	0.005
6H-3, 50	46.30	F	1.198	9.50E-03	0.026
6H-5, 50	49.30	F	1.084	1.40E-02	0.016
7H-1, 50	52.80	F	1.034	1.17E-02	–0.006
7H-3, 50	55.80	F	1.053	9.41E-03	–0.047
7H-5, 50	58.80	F	0.861	1.32E-02	–0.078

Note: Method used either F = full-space or H = half-space, TCcorr = thermal conductivity corrected for drift.

Only a part of this table is reproduced here. The entire table appears on the CD-ROM (back pocket).

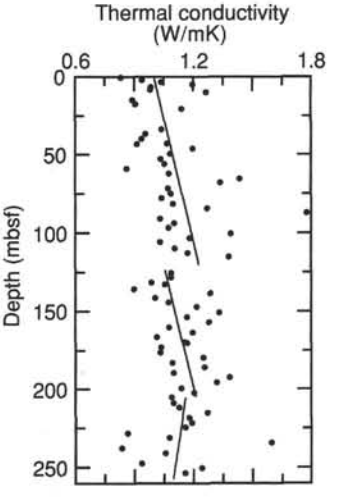

Figure 28. Thermal conductivity, Site 951. Lines represent the best linear fit for each core segment showing different thermal behavior.

Between 2.6 and 6.5 Ma there is a sharp decrease to 2.0 m/m.y. This change in accumulation rate is coincident with the change in pelagic sediments from constant clays below to alternating clays, marls, and oozes above. This change is also seen at Site 950. It coincides with the onset of Northern Hemisphere glaciation, which was accompanied by a sharp lowering of the CCD. The stacked pelagic sediment thickness between zero and 2.6 Ma is 11.39 m at Site 951 compared with 14.6 m at Site 950.

The only age diagnostic data before 6.5 Ma is the occurrence of *Reticulofenestra pseudoumbilicus* at the base of Hole 951B, which has an FO at 13.1 Ma. This suggests that the base of Hole 951B is younger than this age. The only data on which to base an extrapolation of the accumulation rate of pelagic sediments between 6.5 Ma and the base of Hole 951B is that between 2.6 and 6.5 Ma, where a rate of 2 m/m.y. was measured. Since there is a small amount of carbonate present in these sediments, but none in the deeper layers, this

Table 9. Index properties, Holes 951A and 951B.

Core, section, interval (cm)	Depth (mbsf)	WCw (%)	WCd (%)	BDb (g/cm^3)	BDc (g/cm^3)	GDb (g/cm^3)	GDc (g/cm^3)	DDb (g/cm^3)	DDc (g/cm^3)	Porb (%)	Porc (%)	VRb	VRc
157-951A-													
1H-1, 132–134	1.32	60.49	153.12	1.37	1.35	2.83	2.67	0.54	0.53	80.90	79.93	4.24	3.98
1H-2, 99–101	2.49	51.11	104.54	1.48	1.47	2.79	2.69	0.73	0.72	74.04	73.31	2.85	2.75
1H-3, 130–132	4.30	64.16	179.01	1.34	1.32	2.96	2.72	0.48	0.47	83.80	82.63	5.17	4.76
2H-1, 94–96	5.74	53.46	114.85	1.46	1.43	2.84	2.66	0.68	0.67	76.10	74.86	3.18	2.98
2H-2, 118–120	7.48	55.88	126.64	1.42	1.41	2.76	2.68	0.63	0.62	77.32	76.80	3.41	3.31
2H-4, 61–63	9.91	44.90	81.48	1.40	1.55	2.01	2.67	0.77	0.85	61.51	67.96	1.60	2.12
2H-5, 70–72	11.50	44.21	79.25	1.59	1.57	2.83	2.70	0.89	0.87	68.67	67.65	2.19	2.09
2H-6, 140–142	13.70	57.16	133.41	1.39	1.40	2.64	2.71	0.59	0.60	77.46	77.91	3.44	3.53
3H-1, 78–80	15.08	55.22	123.29	1.41	1.42	2.65	2.68	0.63	0.63	76.16	76.36	3.19	3.23
3H-2, 10–12	15.90	54.62	120.34	1.46	1.42	2.95	2.66	0.66	0.65	77.59	75.78	3.46	3.13
3H-3, 127–129	18.57	44.08	78.83	1.59	1.57	2.80	2.72	0.89	0.88	68.29	67.66	2.15	2.09
3H-4, 79–81	19.59	47.71	91.23	1.51	1.52	2.68	2.72	0.79	0.79	70.45	70.78	2.38	2.42
3H-5, 129–131	21.59	49.50	98.02	1.48	1.47	2.59	2.58	0.74	0.74	71.27	71.15	2.48	2.47
3H-8, 21–23	23.15	47.97	92.21	1.51	1.51	2.65	2.70	0.78	0.79	70.49	70.82	2.39	2.43
4H-1, 81–83	24.61	52.02	108.41	1.48	1.45	2.87	2.65	0.71	0.70	75.20	73.72	3.03	2.81
4H-2, 62–64	25.92	51.03	104.23	1.46	1.46	2.64	2.65	0.72	0.72	72.86	72.91	2.69	2.69
4H-3, 43–45	27.23	47.62	90.90	1.54	1.52	2.87	2.71	0.81	0.80	71.80	70.63	2.55	2.40
4H-4, 75–77	29.05	56.22	128.41	1.43	1.41	2.90	2.70	0.63	0.62	78.41	77.21	3.63	3.39
4H-5, 8–10	29.88	56.57	130.25	1.43	1.40	2.95	2.67	0.62	0.61	78.95	77.23	3.75	3.39
4H-6, 124–126	32.54	55.82	126.34	1.44	1.42	2.98	2.73	0.64	0.63	78.62	77.11	3.68	3.37

Notes: WCw = water content (% wet sample weight), WCd = water content (% dry sample weight), BD = bulk density, GD = grain density, DD = dry density, Por = porosity, and VR = void ratio. Suffixes "b" and "c" on column heads indicate value calculated using Method B and Method C, respectively (see "Explanatory Notes," this volume).

Only a part of this table is reproduced here. The entire table appears on the CD-ROM (back pocket).

probably serves as a maximum accumulation rate for these deeper sediments.

Total Sediment Accumulation Rates

The datum levels between zero and 218 mbsf (0–6.5 Ma) give a constant accumulation rate of 33.8 m/m.y. (Fig. 32), which is almost identical to the average accumulation rate for the same interval at Site 950. The absence of data below 217 mbsf (6.5 Ma) prevents any estimations of accumulation rates for the lower part at Site 951. We anticipate being able to add these later following more detailed analyses of both pelagic layers and turbidites.

REFERENCES

Searle, R.C., 1987. Regional setting and geophysical characterization of the Great Meteor East area in the Madeira Abyssal Plain. *In* Weaver, P.P.E., and Thomson, J. (Eds.), *Geology and Geochemistry of Abyssal Plains.* Spec. Publ. Geol. Soc. London, 31:49–70.

Thierstein, H.R., Geitzenauer, K., Molfino, B., and Shackleton, N.J., 1977. Global synchroneity of late Quaternary coccolith datum levels: validation by oxygen isotopes. *Geology,* 5:400–404.

Thomson, J., Colley, S., Higgs, N.C., Hydes, D.J., Wilson, T.R.S., and Sørensen, J., 1987. Geochemical oxidation fronts in NE Atlantic distal turbidites and their effects on the sedimentary record. *In* Weaver, P.P.E., and Thomson, J. (Eds.), *Geology and Geochemistry of Abyssal Plains.* Geol. Soc. Spec. Publ. London, 31:167–178.

Weaver, P.P.E., and Clement, B.M., 1986. Synchroneity of Pliocene planktonic foraminiferal datums in the North Atlantic. *Mar. Micropaleontol.,* 10:295–307.

Weaver, P.P.E., and Kuijpers, A., 1983. Climatic control of turbidite deposition on the Madeira Abyssal Plain. *Nature,* 306:360–363.

Weaver, P.P.E., and Raymo, M.E., 1989. Late Miocene to Holocene planktonic foraminifers from the equatorial Atlantic, Leg 108. *In* Ruddiman, W., Sarnthein, M., et al., *Proc. ODP, Sci. Results,* 108: College Station, TX (Ocean Drilling Program), 71–91.

Wilson, T.R.S, Thomson, J., Hydes, D.J., Colley, S., Culkin, F., and Sørensen, J., 1986. Oxidation fronts in pelagic sediments: diagenetic formation of metal-rich layers. *Science,* 232:972–975.

Young, J.R., Flores, J.-A., and Wei, W., 1994. A summary chart of Neogene nannofossil magnetobiostratigraphy. *J. Nannoplankton Res.,* 16:21–27.

Ms 157IR-105

NOTE: For all sites drilled, core-description forms ("barrel sheets") and core photographs can be found in Section 3, beginning on page 181. Smear-slide and thin-section data are given in Section 4, beginning on page 305. The CD-ROM (back pocket, this volume) contains physical properties and geochemical data, MST data, logging data, and color core photographs (Sites 950 and 953 only).

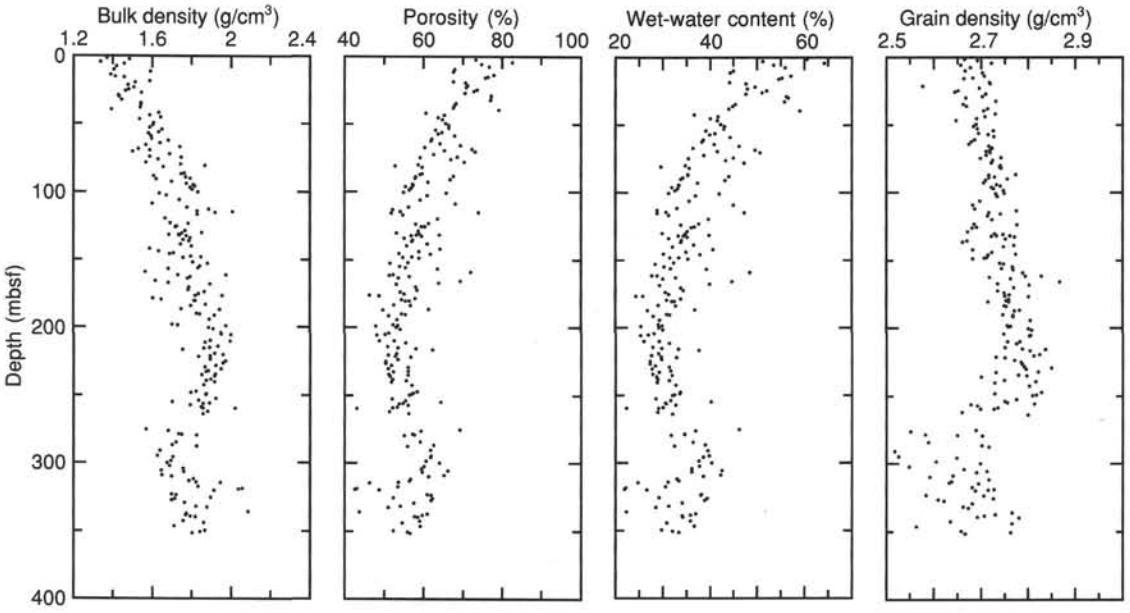

Figure 29. Bulk density (Method B), porosity (Method C), wet-water content, and grain density (Method C), Holes 951A and 951B.

Table 10. Strength measurements, Hole 951A.

Core, section, interval (cm)	Depth (mbsf)	Vane (kPa)	Res (kPa)	Pen (kPa)
157-951A-				
1H-1, 130–131	1.30	5	0	
1H-2, 98–99	2.48	6	3	
1H-3, 135–136	4.35	5	2	
2H-1, 95–96	5.75	9	4	
2H-2, 119–120	7.49	7	4	
2H-4, 63–64	9.93	14	8	
2H-5, 70–71	11.50	2	1	
2H-6, 140–141	13.70	12	7	
3H-1, 81–82	15.11	11	6	
3H-2, 11–12	15.91	19	7	
3H-3, 124–125	18.54	9	4	
3H-4, 81–82	19.61	15	8	
3H-5, 131–132	21.61	22	9	
3H-8, 24–25	23.18	18	9	
4H-1, 83–84	24.63	25	11	
4H-2, 64–65	25.94	25	11	
4H-3, 44–45	27.24	24	16	
4H-4, 78–79	29.08	17	8	
4H-5, 11–12	29.91	13	6	
4H-6, 127–128	32.57	21	8	

Note: Vane = undrained shear strength as measured by the vane shear, Res = residual shear strength, and Pen = unconfined shear strength as measured by the penetrometer, converted to kPa.

Only a part of this table is reproduced here. The entire table appears on the CD-ROM (back pocket).

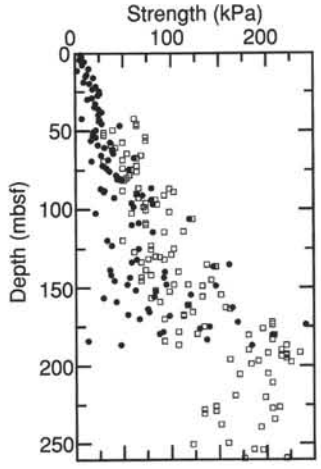

Figure 30. Strength data determined by vane shear (filled circles) and hand-held penetrometer methods (open squares), Hole 951A.

Table 11. Datum levels used in calculation of sediment accumulation rate curves.

	Event	Sample Top	Sample Bottom	Depth (mbsf) Top	Depth (mbsf) Bottom	Pelagic depth (m) Top	Pelagic depth (m) Bottom	Age (Ma)
		157-951A-	157-951A-					
1	LO *P. lacunosa*	3H-7, 8	4H-4, 18	22.38	28.48	2.32	2.76	0.46
2	Brunhes/Matuyama boundary	4H-3, 15	—	27	—	2.56	—	0.78
3	LO *R. asanoi*	4H-6, 18	4H-4, 18	28.48	31.48	2.76	3.1	0.83
4	Jaramillo top	5H-4, 50–65	—	38	—	3.79	—	0.99
5	FO *R. asanoi*	4H-6, 18	5H-5, 72	31.48	40.02	3.1	3.96	1.06
6	FO *G. oceanica*	4H-6, 18	5H-5, 72	31.48	40.02	3.1	3.96	1.08
7	LO *Gephyrocapsa* spp. (>4 µm)	5H-6, 84.5	6H-4, 5	41.65	47.35	4.01	6.84	1.24
8	Olduvai top	7H-5, 60	—	59	—	7.33		1.77
9	FO *G. caribbeanica*	7H-5, 63	8H-5, 45.5	58.93	67.76	7.35	9.19	1.8
10	FO *G. truncatulinoides*	8H-5, 52–54	8H-6, 75–77	67.82	69.55	9.25	9.65	1.92
11	LO *D. brouweri*	7H-5, 63	8H-5, 45.5	58.93	67.76	7.35	9.19	1.95
12	Olduvai bottom	8H-4, 90	—	67.5	—	8.95	—	1.95
13	FO *D.triradiatus* acme	8H-6, 81	9H-6, 62	69.61	79.42	9.73	10.97	2.15
14	FO *G. inflata*	8H-6, 75–77	9H-6, 62–64	69.55	79.42	9.65	10.99	2.19
15	Gauss top	10H-5, 40	12H-1, 15	80	87	11.39	—	2.6
16	LO *D. surculus*	9H-7, 7.5	10H-5, 37	80.38	87.17	11.18	11.42	2.61
17	LO *D. tamalis*	10H-6, 16	11H-4, 148	88.46	96.28	11.47	11.82	2.76
18	LO *R. pseudoumbilicus*	15X-1, 119	15X-CC, 5	126.19	132.21	12.79	13.52	3.77
19	FO *D. tamalis*	16X-2, 53.5	16X-5, 64	133.24	137.84	13.84	14.02	4.01
20	LO *Amaurolithus* spp.	16X-5, 64	17X-6, 60	137.84	148.9	14.02	15.04	4.39
21	FO *D. asymmetricus*	19X-2, 119	19X-6, 3	162.79	167.63	16.05	16.34	4.79
22	LO *D. quinqueramus*	21X-6, 29.5	21X-CC, 1	187.2	188.83	17.26	17.3	5.56
23	LO *A. amplificus*	23X-5, 16	23X-5, 49	204.86	205.19	17.93	17.97	5.88
24	FO *A. amplificus*	24X-6, 102	24X-CC, 17.5	216.92	217.58	18.75	18.94	6.5
		157-951B-						
25	FO *R. pseudoumbilicus*	10X-CC, 23	—	351.13	—	25.13	—	13.1

Notes: Numbers in left column match numbers on Figures 31 and 32. The pelagic depths refer to the depth of datum levels in the stacked pelagic sequence.

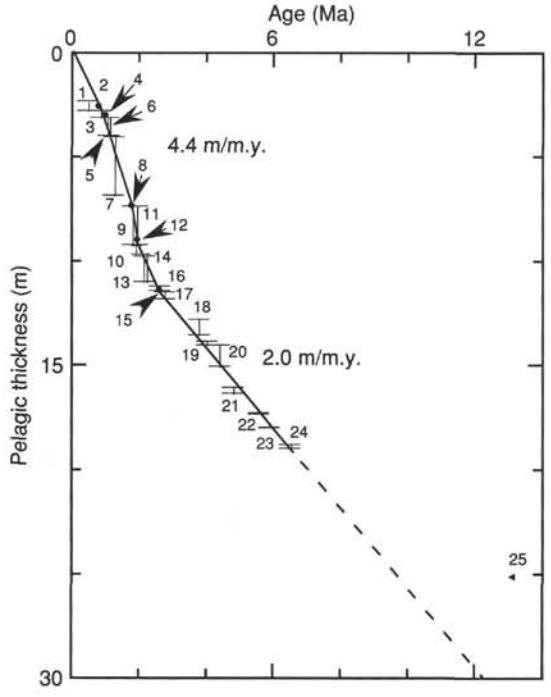

Figure 31. Sediment accumulation rates for the pelagic sequence of Holes 951A and 951B. Vertical bars represent distances between sample points. Numbers refer to datum levels given in Table 11.

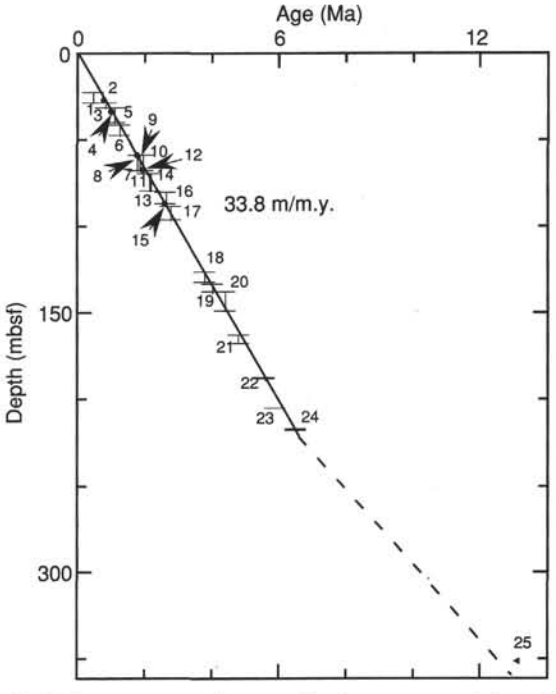

Figure 32. Sediment accumulation rates for the upper part of the total sediment sequence of Holes 951A and 951B. Vertical bars represent distances between sample points. Numbers refer to datum levels given in Table 11.